INVESTIGATION AND CHARACTERIZATION OF CARBON FILMS SPUTTERED ON SILICA AEROGEL MONOLITHS

NIKNAZ ATASH DEHGHAN

A THESIS SUBMITTED TO THE FACULTY OF GRADUATE STUDIES
IN PARTIAL FULFILMENT OF THE REQUIREMENTS
FOR THE DEGREE OF
MASTER OF APPLIED SCIENCE

GRADUATE PROGRAM IN MECHANICAL ENGINEERING
YORK UNIVERSITY
TORONTO, ONTARIO

APRIL 2026

Abstract

This study investigates the deposition of a 500 nm carbon (C) layer onto hydrophilic bare silica aerogels (BSA) using the magnetron sputtering method. By leveraging the mesoporous structure of silica aerogel, a carbon-coated aerogel nanocomposite was produced. Spectroscopic characterization of the resulting nanocomposite revealed ultraviolet scattering behavior, enhanced visible light absorption, and changes in optical transmittance. FTIR spectroscopy further demonstrated that the carbon layer reduced transmittance in the near-infrared (NIR) and mid-infrared (MIR) regions. Infrared thermal imaging confirmed a photothermal response, where samples coated with a 500 nm carbon layer reached temperatures up to 59 °C under simulated solar irradiation at an intensity of 100 mW/cm². Solar absorptance calculations further showed an increase from approximately 6.9% for BSA to 75.8% for CSSA, indicating enhanced solar energy absorption after carbon sputtering. In addition, carbon capture experiments were performed to evaluate the influence of carbon sputtering on CO_2 adsorption and desorption behavior. The findings demonstrate that carbon sputtering modified the optical and photothermal properties of silica aerogels and provided insight into their potential use in carbon capture applications.

Acknowledgements

I would like to express my sincere gratitude to my supervisors, Dr. Paul G. O'Brien and Dr. Thomas Cooper, for their invaluable guidance, support, and encouragement throughout my research journey. Their mentorship helped shape both my technical understanding and professional growth.

I am also thankful to the members of the AM-SET-Lab and Cooper labs, and to the skilled technicians who assisted me with equipment and procedures. Their time and knowledge were essential to the completion of this work.

I extend my heartfelt thanks to my friends who stood by me during this challenging journey with their kindness, encouragement, and patience.

Lastly, I have the deepest appreciation for my parents, Masoud and Shokofeh. Their unwavering support, strength, and belief in me have been the foundation of this accomplishment. This milestone would not have been possible without them.

Table of Contents

List of Tables

List of Figures

Abbreviations

ALD	Atomic Layer Deposition
BSA	Bare Silica Aerogel
CVD	Chemical Vapor Deposition
CSSA	500 nm C on Bare Silica Aerogel
DT	Direct Transmission
FTIR	Fourier Transform Infrared
HT	Hemispherical Transmission
IS	Integrating Sphere
MS	Magnetron Sputtering
NP	Nanoparticle
PVD	Physical Vapor Deposition
TR	Total Reflection
TEOS	Tetraethyl Orthosilicate
TMOS	Tetramethyl Orthosilicate
UV-Vis	Ultra-Violet Visible
UV	Ultra-Violet

Nomenclature

Chemical Formulae

Al_2O_3	Aluminum Oxide (Alumina)
Ar	Argon
C	Carbon

Chapter 1 -Introduction

1.1 Global Climate Change and the Urgency of Action

Our planet is experiencing an alarming and accelerating warming trend. Rising global temperatures are primarily attributed to the accumulation of greenhouse gases (GHGs) in the atmosphere, with carbon dioxide (CO_2) being the most dominant contributor [1]. The consequences of this warming are far-reaching and already visible, including the melting of glaciers, rising sea levels, more frequent and intense floods, droughts, and hurricanes [2]. These climatic shifts pose serious threats to human health, ecosystems, food security, and global economic stability, making climate change one of the most pressing challenges of the twenty-first century [3].

To address this global crisis, international cooperation has become essential. A landmark response was the signing of the Paris Agreement in 2015, which brought together nearly all countries in a unified effort to mitigate climate change. Its central objective is to limit global warming to well below 2 °C above pre-industrial levels, while pursuing efforts to restrict the rise to 1.5 °C [4-5]. Achieving this target requires not only reducing GHG emissions but also developing and implementing innovative, scalable technologies for carbon management, such as the development of effective CO_2 capture technologies.

1.2 Carbon Dioxide Capture Strategies

Carbon dioxide accounts for approximately three-quarters of anthropogenic GHG emissions and is widely recognized as the primary driver of climate change [6]. Therefore, reducing atmospheric CO_2 concentrations is critical to slowing global warming. Several technologies have been developed to capture and manage CO_2 [7], which can broadly be categorized into the following approaches:

Absorption: Chemical solvents, such as amine-based solutions, absorb CO_2 through reversible reactions. Although effective, these processes are energy intensive and present challenges of solvent degradation and corrosion [8].

Adsorption: Solid sorbents, including zeolites, activated carbons, and advanced porous materials, selectively capture CO_2 on their surfaces. Adsorption offers advantages such as regenerability, modular design, and lower energy penalties compared to liquid absorption [9].

Membrane Separation: Polymeric, ceramic, or hybrid membranes selectively separate CO_2 from gas mixtures. These systems are compact and energy-efficient but can be limited by selectivity and scalability [10-11].

Cryogenic Distillation: Cooling and compressing flue gases to extremely low temperatures separates CO_2 as a liquid. While highly pure CO_2 can be obtained, the process is costly and energy demanding [12]. Among these options, adsorption using solid materials has emerged as a particularly promising pathway due to its tunable surface chemistry, mechanical robustness, and compatibility with renewable energy integration [13].

Of the aforementioned CO_2 capture strategies, using solid adsorbents is particularly attractive due to their energy efficiency, selectivity, and reduced operating costs compared to other common approaches that use chemical solvents. Furthermore, recent research has been directed towards photothermal regeneration of solid adsorbents [59-63]. In this approach solid sorbents that capture CO_2 using temperature swing adsorption cycles are heated photothermally using incident light energy rather than traditional heat sources derived from fossil fuels. Adsorbents can be infused into porous supports that are heated using light sources such as LEDs or incident solar radiation. Silica aerogels are a promising support for CO_2 adsorbents due to their light weight, high porosity and high specific surface area.

1.3 Silica Aerogels as Advanced Adsorbent Supports

Silica aerogels are ultra-lightweight, porous solids with exceptional surface area-to-volume ratios, low density, and outstanding thermal insulation properties. These unique characteristics make them excellent support structures for gas adsorption applications, including CO_2 capture [14]. By providing a highly porous matrix, silica aerogels enable efficient diffusion and binding of gas molecules, while their tunability allows for surface modification to optimize performance [15].

However, bare silica aerogels (BSA) possess a critical drawback for photothermally driven processes: they are optically transparent and weakly absorbing in the visible spectrum, limiting their effectiveness in applications where light-to-heat conversion is essential [16]. This deficiency restricts their use in photothermal-driven CO_2 capture systems, where efficient solar absorption and subsequent heat transfer are required to regenerate sorbents and sustain long-term operation [17].

1.4 Enhancing Aerogels Through Surface Modification

To overcome these limitations, researchers have developed strategies to incorporate light-absorbing components into silica aerogels. Approaches include impregnating the aerogel with carbon black, metal nanoparticles, or organic dyes. While effective, these methods often compromise porosity or introduce structural fragility [18].

An alternative strategy is carbon sputtering [19], which is a physical vapor deposition (PVD) [20] technique in which a thin, uniform layer of carbon is deposited onto the aerogel surface. This modification enhances optical absorption without significantly altering the aerogel's lightweight structure or pore architecture. The sputtered carbon layer introduces two key advantages:

1. Improved optical absorption: Enhanced broadband light absorption enables efficient solar-to-thermal energy conversion.
2. Enhanced thermal conduction: The carbon layer facilitates uniform heat distribution across the aerogel framework, preventing localized hot spots and improving stability during repeated heating–cooling cycles [21].

1.5 Research Motivation

The motivation for this research arises from the need to develop sustainable materials for CO_2 capture. In this regard, recent research has been directed towards using incident light to regenerate CO_2 adsorbents. A promising approach to light-driven CO_2 capture is to infuse CO_2 adsorbents into the pores of photothermal supports. These supports can be heated by incident light, such as solar radiation, to raise their temperature and regenerate the CO_2 adsorbents as part of a temperature-swing adsorption CO_2 capture process. Silica aerogels have high potential to be

effective supports for CO_2 adsorbents due to their light weight, high specific surface area, and low thermal conductivity. However, bare silica adsorbents are not effective photothermal materials when subjected to incident radiation in the solar region due to their low adsorption over this range. While bare silica aerogels provide excellent structural advantages, their limited optical absorption reduces their potential in solar-driven CO_2 capture applications. In this research, to increase the adsorption of silica aerogels, thin carbon films are sputtered onto their surface. The silica aerogels with carbon films deposited onto their surface, referred to as carbon-sputtered silica aerogels (CSSA), are characterized in terms of their optical and photothermal properties. Furthermore, experiments are conducted using a dynamic adsorption/desorption breakthrough apparatus to evaluate their performance in solar-driven CO_2 capture applications.

1.6 Research Objectives

This thesis aims to:

1. Synthesize silica aerogels via sol–gel processing and prepare carbon-sputtered silica aerogels through magnetron sputtering.
2. Characterize the structural and optical properties of BSA and CSSA using FTIR and UV–Vis spectroscopy.
3. Evaluate the photothermal performance of CSSA relative to BSA under simulated solar illumination.
4. Explore implications for CO_2 capture, focusing on how carbon sputtering improves aerogel performance as an integrated solar-thermal adsorbent.

1.7 Overview of Thesis Structure

This thesis is organized as follows:

Chapter 1 introduces the global context of climate change, the importance of carbon dioxide capture, and the motivation behind modifying silica aerogels through carbon sputtering.

Chapter 2 presents a comprehensive literature review on CO_2 capture technologies, aerogels, and physical vapor deposition techniques.

Chapter 3 describes the experimental methodology, including the preparation of BSA and CSSA, and the characterization techniques employed.

Chapter 4 discusses results from optical, photothermal, and CO_2 capture testing, highlighting performance comparisons between BSA and CSSA.

Chapter 5 summarizes the conclusions and outlines recommendations for future research.

Chapter 2 -Background Information

2.1 Carbon Capture

Carbon capture and storage (CCS) is a vital strategy in global efforts to mitigate climate change. By capturing carbon dioxide (CO_2) emissions at their source and preventing their release into the atmosphere, CCS helps reduce the accumulation of GHG responsible for global warming. The urgency of climate action, coupled with the commitment of many countries to reduce their carbon emissions, has positioned CCS technologies at the forefront of environmental research and policy.

In addition to industrial point-source capture, recent developments have emphasized direct air capture (DAC), where CO_2 is removed directly from ambient air. Although energy-intensive, DAC provides the unique advantage of addressing dispersed emissions and offers a pathway toward negative emissions when coupled with permanent storage or utilization [22]. In this work photothermal adsorbents comprised of carbon sputtered on silica aerogels are fabricated, characterized and tested with the aim of developing adsorbents for photothermal CO_2 capture. Background information relevant to the research carried out in this thesis are provided in the following paragraphs.

2.1.1 The Historical Development of Carbon Capture

The concept of CO_2 capture dates back to the early 20th century, when technologies for gas purification and natural gas processing were first developed. One of the earliest demonstrations of CO_2 removal involved the use of alkaline solutions to scrub CO_2 from gas streams [23].

The role of carbon capture in mitigating climate change grew significantly in the late 20th century, as the scientific consensus around anthropogenic global warming became established. This was reinforced through international agreements such as the Kyoto Protocol (1997) [24] and the Paris Agreement (2015), which emphasized reducing emissions from industrial sectors. These

milestones drove research and development efforts aimed at advancing capture technologies and scaling them for large-scale deployment [25].

2.1.2 Current Status and Methods of Carbon Capture

Carbon capture methods are generally classified into four categories:

1) Post-combustion capture: Removes CO_2 from flue gases after fossil fuel combustion, typically using solvents or solid sorbents.
2) Pre-combustion capture: Processes the fuel before combustion to generate a CO_2 rich stream that can be separated.
3) Oxy-fuel combustion: Burns fuel in pure oxygen to produce a highly concentrated CO_2 stream[26].
4) Direct Air Capture: CO_2 is extracted directly from the air for storage or utilization.

Among these, post-combustion methods [27] are the most widely adopted because they can be retrofitted into existing power plants and industrial facilities. Technologies employed include chemical absorption (amine solvents), solid adsorption, and membrane separation. Direct air capture (DAC) is also emerging as a complementary method to address diffuse CO_2 sources.

Unlike traditional carbon capture, DAC facilities are not dependent on a fixed emission source and can be deployed in a variety of locations. Given the challenge of addressing historical and hard-to-abate GHG emissions (such as those from aviation), DAC is considered a necessary tool for reaching global net-zero targets.

2.1.3 Solid Adsorbents for Carbon Capture

Solid adsorbents have gained significant attention as alternatives to liquid amine-based systems because of their stability, lower energy regeneration costs, and tunable structures. Examples of solid adsorbents used for CO_2 capture include zeolites, activated carbons, and metal-organic frameworks (MOFs), and amine-functionalized porous solids [28]. Their high surface areas and customizable pore sizes enable efficient CO_2 adsorption and selective gas separation. However, large-scale deployment requires further advances in stability under real-world conditions and in regeneration efficiency [29].

2.1.4 The Temperature Swing Adsorption Process

Temperature Swing Adsorption (TSA) methods are typically employed when using solid adsorbents to capture CO_2. In the TSA process, the cycle of adsorbing CO_2, desorbing CO_2, and subsequently releasing it is achieved through a change in temperature. First, the adsorbent is exposed to a gas stream containing CO_2 at a low temperature (often ambient temperature) so that CO_2 molecules are adsorbed onto its surface. Then, for the regeneration step, the adsorbent's temperature is increased; with the rise in temperature, the physical or chemical bonds between the CO_2 and the adsorbent surface are broken, and the CO_2 is released at an elevated concentration, making the adsorbent ready for the next cycle. For example, studies that have used carbon-based materials (such as activated charcoal, carbon nanotubes, or porous carbon frameworks) for carbon capture have utilized the following regeneration temperatures:

1. In a study focused on modified activated carbons, the complete regeneration of the adsorbent and the release of captured CO_2 was successfully achieved at a temperature of 100 °C. This relatively low temperature significantly reduces the energy consumption of the DAC process.[31-35]
2. Some other articles that utilized nitrogen-enriched porous carbon frameworks used a higher temperature, such as 120 °C to 130 °C, for CO_2 desorption, to ensure high efficiency and fast regeneration. [31-35]
3. Furthermore, in cases where the goal was maximum and rapid CO_2 removal, articles have shown carbon nanotube materials being exposed to higher temperatures, around 150 °C, for regeneration. [31-35]

The choice of the precise regeneration temperature in the TSA process depends directly on the type of carbon adsorbent, its chemical modification method, and the structural stability of the material, but in most cases, the target temperature for carbon-based materials is within the range of 90 °C to 150 °C.

2.2 Carbon-Silica Composite Aerogels as a Support Material for CO_2 Adsorbents

Silica aerogels are highly porous, lightweight solids with surface areas often exceeding 600–1000 m^2/g, pore volumes of 2–4 cm^3/g, and bulk densities as low as 0.003–0.2 g/cm^3. These exceptional

properties make them suitable as support matrices for dispersing functional nanoparticles or catalytic coatings. Their structure allows gas molecules to diffuse easily and interact with embedded active sites, making silica aerogels promising candidates for hybrid adsorbent systems[30].

2.2.1 Aerogel Fabrication Process

Silica aerogels are typically fabricated using the "sol-gel" process [36]. A "sol" comprises tiny particles dispersed in a liquid and a gel is a "semi-solid" material consisting of a three-dimensional network of solid particles. In gels the space within the particle network is typically filled with a liquid. However, in aerogels the liquid is removed and air resides within the pores of the network. Removing the liquid during aerogel fabrication is a delicate process that must be done carefully to prevent the network from collapsing.

2.2.1.1 Sol-Gel and Gelation

The process begins with the preparation of a sol; a stable colloidal suspension where solid particles (typically metal oxide or silica) are uniformly dispersed in a liquid solvent (often an alcohol). When fabricating silica aerogels the sol is typically comprised of a silicon alkoxide precursor, such as tetraethyl orthosilicate (TEOS) or tetramethyl orthosilicate (TMOS), mixed with a solvent consisting of alcohol and water. Silonal is formed via a hydrolysis reaction whereby a catalyst (such as ammonia or hydrochloric acid) is used to induce water to react with the precursor to form silanol groups.

During the subsequent gelation process the silanol groups form siloxane bonds. The duration of the gel time depends on the conditions (pH and temperature) and can vary considerably, lasting from a few minutes to days. The formed gel is a continuous, three-dimensional network of solid particles that spans the entire volume of the former sol, with its internal space filled by the solvent. At the gel point, the entire system can no longer flow, as a solid network with weak mechanical strength has been formed.

The selection of catalyst has significant effects on the hydrolysis reaction. Base catalysts, such as ammonia, drastically increase the rate of the condensation reaction. A fast condensation reaction causes a faster gelation process which leads to the formation of larger particles with lower density.

On the other hand, acid catalysts increase the rate of the hydrolysis reaction, often resulting in the formation of smaller particles and denser gels.

Another important parameter to control during the aerogel fabrication process is the gelation time. The gel time significantly impacts the final microstructure of the aerogel. A short gel time (fast gelation) often leads to the formation of denser clusters and larger particles, which may not yield a uniform porous structure. Alternatively, long gel times (slow gelation) allows more time for particle growth and restructuring, usually resulting in a stronger more uniform network structure with controlled porosity. Therefore, precise control over parameters such as catalyst concentration and temperature is crucial to achieve the optimal gelation time necessary for synthesizing aerogels with desired properties (e.g., low density, high surface area, and appropriate mechanical strength).

2.2.1.2 Supercritical Drying in the Aerogel Fabrication Process

Supercritical drying (SCD) is a process designed to remove liquid solvent from a gel without inducing capillary stresses that typically cause structural collapse. This is achieved by bringing the solvent often CO_2 beyond its critical temperature (31.1 °C) and pressure (7.38 MPa), into a supercritical state. In this condition, CO_2 behaves as both a gas and a liquid, allowing it to displace and extract solvent from the pores of the gel without crossing a liquid-gas interface.

In practice, to implement SCD, the drying chamber is initially pressurized to 8–10 MPa while maintaining a temperature of approximately 40–45 °C. Once equilibrium is reached, the pressure is slowly reduced, converting supercritical CO_2 to gas and enabling its exit from the system without damaging the gel structure. This method is widely regarded as the gold standard for producing crack-free, porous aerogels.

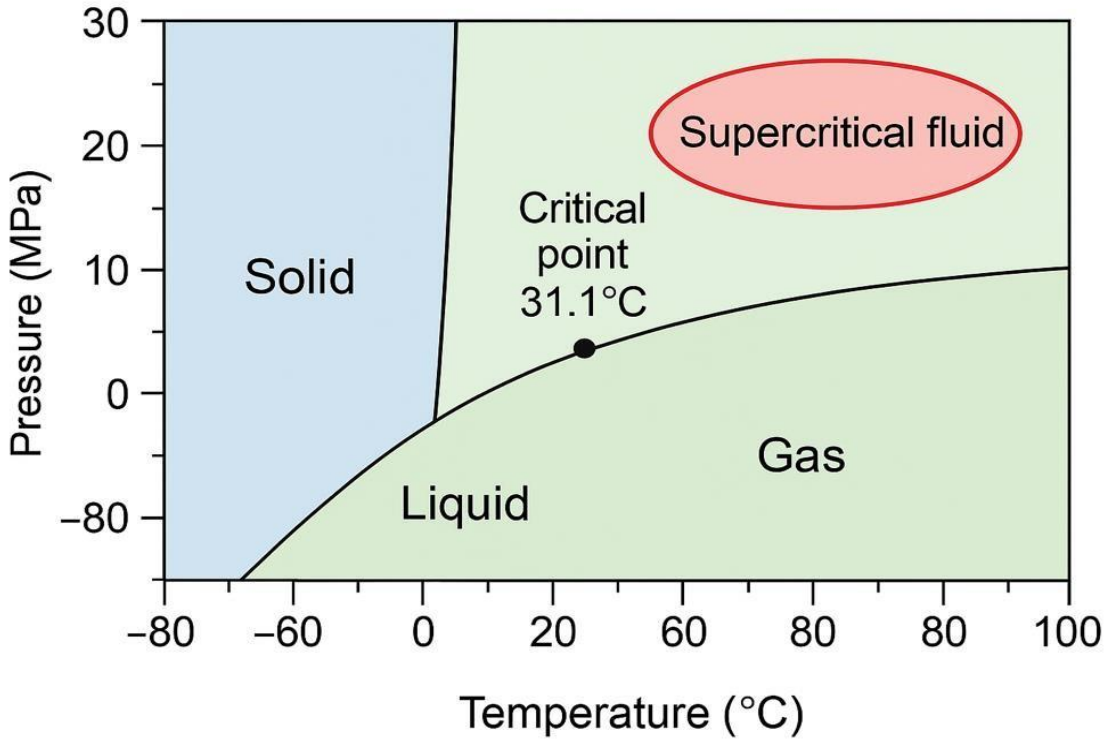

Figure 2.1 Phase diagram of carbon dioxide showing the transition into the supercritical region above 31.1 °C and 7.38 MPa. Supercritical CO_2 is used in aerogel drying to prevent structural damage due to surface tension forces.

2.2.1.3 Limitations of the Sol-Gel Aerogel Fabrication Process

The sol-gel process has established itself as the predominant method for synthesizing and producing inorganic aerogels, holding a unique position in this field. However, the application of this method to the fabrication of aerogels containing metallic nanoparticles is fraught with significant challenges and obstacles. One of the most critical challenges is the inherent instability of the sol-gel reaction itself [37]. Instability arises because the reaction is highly susceptible to various factors such as temperature, pH, catalyst type, and precursor concentrations, demanding extremely precise control. Furthermore, the complexities inherent in the sol-gel reaction mechanism, especially in the presence of metallic nanoparticles, render the prediction and control of the final aerogel properties difficult. Consequently, a thorough investigation and evaluation of fabrication parameters or alternative methods to overcome these limitations and achieve higher-quality aerogels with more desirable properties is imperative [38].

As an example, Shao et al.'s study on carbon-titanium dioxide composite samples aptly underscores the time-consuming nature of the sol-gel process. In their research, samples were subjected to a constant temperature of 70 °C for five days to form the wet gel structure. Subsequently, these samples underwent SCD under precise temperature and pressure conditions to completely remove the internal moisture. Afterward, the samples were carbonized at high temperatures to enhance strength and improve properties. In total, the entire process spanned one week [39]. The fabrication of metallic aerogels necessitates a higher level of complexity and attention to detail due to their inherent characteristics. In these aerogels, meticulous selection of the size, shape, and composition of pre-synthesized nanostructures is crucial. Additionally, precise control over the gelation process is essential to achieve a well-ordered and stable structure. Lázár et al.'s study highlights the challenges associated with synthesizing silica aerogels containing gold nanoparticles. Minor variations in experimental conditions, such as the type of solvent or gas composition, can lead to significantly different outcomes [40].

2.2.2 Structural Challenges in Aerogels

Despite their advantages, aerogels suffer from drawbacks such as shrinkage, cracking, and fragility during synthesis and drying. Even with techniques like autoclave SCD, microcracks can form, especially in the presence of nanoparticles. These cracks hinder performance and reduce mechanical integrity [41]. To address this, researchers employ thermal treatments and surface modifications. For example, Ferreira-Neto et al. demonstrated that careful solvent exchange, followed by supercritical drying and controlled heating, reduced shrinkage and improved stability [42]. Surface coatings (e.g., carbon or polymer layers) can also impart additional structural stability, protecting the fragile aerogel framework from capillary collapse [43-44].

2.2.3 Carbon-Modified Aerogels and their Advantages

Recent research has explored modifying silica aerogels with carbon-based materials such as graphene, nanotubes, or thin carbon films via sputtering [45]. These modifications provide two main benefits:

1. Enhanced thermal conductivity, improving heat distribution within the aerogel[46].
2. Increased light absorption, enabling efficient solar-to-thermal conversion and regeneration of CO_2 sorbents.

In this research, a ~500 nm carbon film was deposited on silica aerogels using magnetron sputtering, improving optical and thermal properties while maintaining porosity [47].

2.2.3.1 Scalability and Practical Challenges of Aerogel-Based Adsorbents

Despite the advantages listed in the previous section, silica aerogels still face important practical limitations that restrict their widespread industrial implementation for CO_2 capture. Aerogel fabrication commonly involves time-consuming sol-gel synthesis, multiple solvent exchange stages, and specialized drying processes, all of which increase production complexity and cost. In addition, aerogels are mechanically fragile and may suffer from structural degradation during repeated adsorption-desorption cycles, particularly under thermal cycling conditions.

As a result, although silica aerogels provide highly controlled and well-defined porous structures that are valuable for laboratory scale research and proof of concept investigations, other support materials such as activated carbons, zeolites, silica gels, and amine-functionalized porous solids may currently offer more practical and economically feasible solutions for large-scale CO_2 capture systems. Nevertheless, ongoing advances in aerogel manufacturing methods, reinforcement strategies, and recyclable hybrid materials may improve the future scalability and commercial viability of aerogel-based adsorbents.

2.2.4 Physical Vapor Deposition and Sputtering Techniques

Physical Vapor Deposition (PVD) enables controlled fabrication of thin films. In sputtering, gas ions bombard a target material, ejecting atoms that are then deposited as a thin coating on a substrate [48]. Magnetron sputtering enhances this process by applying a magnetic field, increasing plasma density, and improving deposition rates [49]. DC sputtering employs direct current for gas ionization, often used for conductive materials [50]. RF sputtering uses high-frequency alternating current, typically for insulating materials. Magnetron sputtering allows precise control of thin-film thickness, surface morphology, and uniformity, making it highly versatile for engineering coatings on porous structures like aerogels. However, challenges such as arcing, pinhole formation, and stress-induced cracks must be carefully managed. [51]

2.3 Summary of Literature Gaps

Although a wide variety of adsorbents have been studied for CO_2 capture, relatively few have focused on carbon-sputtered silica aerogels. The unique combination of high porosity, low density,

and enhanced optical absorption from carbon coatings represents a promising but underexplored pathway for CO_2 adsorption and photothermal regeneration. This thesis addresses this gap by systematically characterizing the photothermal and adsorption properties of bare silica aerogels and their carbon-sputtered counterparts, contributing new insights into their potential for sustainable energy and climate applications [54].

Chapter 3 -Methodology

This chapter outlines the methodology employed in the synthesis, modification, and characterization of silica aerogels. Section 3.1 describes the fabrication and procurement of silica aerogels, including both the in-lab wet gel synthesis and the commercially sourced aerogels used for testing. Section 3.2 details the characterization techniques applied to the bare silica aerogels (BSA) and carbon-sputtered silica aerogels (CSSA), including UV-Vis spectroscopy, FTIR analysis, thermal imaging, and CO_2 capture testing. The parameters, instruments, and procedures used in each experiment are specified to ensure reproducibility and clarity.

3.1 Aerogel Fabrication

This section describes the fabrication of silica aerogels using a sol-gel process based on tetramethyl orthosilicate (TMOS). The synthesis protocol followed was based on established methods (Zhao et al., 2019) and implemented in the Cooper Lab under standard laboratory conditions. The wet gel preparation was completed successfully and used to investigate gelation behavior under varying catalyst concentrations and aging durations, which is further discussed in Chapter 4. Due to limitations in drying infrastructure, the final aerogel samples used for testing were commercially sourced. These samples underwent post-processing via carbon sputtering prior to characterization and CO_2 capture testing.

3.1.1 Wet-Gel Synthesis Procedure

The synthesis of silica aerogel via the sol-gel method involved a series of controlled steps designed to form a robust 3D gel network. All experiments were conducted using a Standard Operating Procedure (SOP) developed by the author based on protocols established in the Cooper Lab, adapted from Zhao et al., 2019.

In a typical preparation, tetramethyl orthosilicate (TMOS) was used as the silica precursor and mixed with methanol under vigorous stirring. Separately, deionized water and ammonia solution

(NH_3, 2.0 M in methanol), used as the base catalyst, were premixed and added dropwise to the TMOS–methanol solution under continuous stirring. The final molar ratio in the standard formulation was:

TMOS : MeOH : H_2O : NH_3 = 1 : 6.42 : 4 : 0.0348

This corresponds to approximate effective concentrations in the final sol of 2.07 M (TMOS), 13.3 M (MeOH), 8.39 M (H_2O), and 0.068 M (NH_3).

To prepare a single batch, the following volumes were used: 10 mL TMOS, 16 mL methanol, 4.9 mL DI water, and 1.1 mL ammonium hydroxide (2.0 M in methanol) all at room temperature.

After the catalyst addition, gelation began within approximately 10–20 minutes. The sol was quickly poured into shallow aluminum dish molds (6 cm diameter × 1.5 cm height) that had been cleaned and pre-labelled. These dishes served as both gelation containers and solvent exchange vessels, ensuring minimal handling of the fragile wet gels. The gels remained inside these aluminum molds throughout the subsequent processing steps. After initial gelation, a thin layer of methanol was gently added to cover the gel surface to prevent drying. The dishes containing the gels were then placed into sealed jars for the aging step at room temperature (~22 °C) for 24 h.

Following aging, the samples (still inside the aluminum molds) were immersed directly into large airtight borosilicate glass containers (approximately 1.5 to 2 L in volume) containing methanol and soaked for 24 h. This was followed by multiple ethanol solvent exchanges (at least four times over a period of 5 to 14 days) using fresh ethanol each time. At larger, industrial scales, this process can be significantly accelerated using continuous solvent exchange systems and optimized diffusion conditions, although the underlying mechanism remains the same. This multistep washing process served to remove unreacted precursors and byproducts and to reinforce the mechanical integrity of the gel network prior to drying. The gel formation process was governed by hydrolysis and condensation reactions initiated by the sol-gel chemistry, using TMOS as the silicon source and ammonia (NH_3) as the base catalyst.

To investigate the effect of catalyst concentration on the gelation kinetics, six different volumes of the 2.0 M ammonia solution in methanol were tested (0.05–2.0 mL), corresponding to different catalyst concentrations in the sol: 0.05, 0.1, 0.25, 0.5, 1.1, and 2.0 mL. For each ammonia volume, the gelation time was measured after three distinct catalyst aging time: 60 s, 300 s, and 3600 s.

Each test condition was repeated three times to ensure statistical accuracy and reproducibility. The average gelation time for each condition was calculated and used for comparative analysis. During this period, a separate study was also conducted to monitor gelation time as a function of both catalyst concentration and aging duration. These results are presented in Chapter 4.

3.1.2 Supercritical Drying

Despite successfully completing the synthesis stage, drying the wet gels into monolithic aerogels was not achieved due to technical limitations associated with the Tousimis AUTOSAMDRI-931 supercritical dryer. The standard drying procedure, as detailed in the lab's SOP, involves multiple cycles of CO_2 filling, purging, and extended stasis holds to enable gradual and complete ethanol–CO_2 exchange prior to reaching supercritical conditions.

For optimal performance, each gel sample must remain submerged in liquid CO_2 under static conditions for 24 h per stasis cycle, typically repeated three times. However, during multiple drying attempts, the system consistently encountered leak-related errors, particularly during prolonged stasis periods. These leaks disrupted chamber pressure and prevented the samples from maintaining the necessary equilibrium conditions.

To troubleshoot the issue, the stasis time was incrementally reduced from 24 h to 2, 4, and 6 h, in an effort to bypass the leak trigger and allow partial ethanol exchange. In each trial, the chamber was filled, purged, and held for shorter intervals while maintaining as close to supercritical conditions as possible. While these modified cycles allowed partial drying, they were ultimately insufficient to fully remove the solvent or preserve the gel's monolithic structure. Representative images of the partially dried silica aerogels obtained from in-lab supercritical drying attempts are shown in Figure 3.1. All samples exhibited significant shrinkage or collapse, likely due to residual ethanol and incomplete supercritical transition.

Figure 3.1 Representative images from in-lab attempts to dry silica wet gels using the Tousimis AUTOSAMDRI-931 supercritical dryer. Challenges such as leakage and difficulty maintaining stable stasis conditions resulted in partial drying and structural changes in the gel network. The images show typical outcomes, including surface cracking, shrinkage, and network separation. These observations contributed to the decision to use commercially dried aerogel monoliths for subsequent testing.

This persistent equipment limitation rendered in-lab drying unsuccessful, leading to the decision to discontinue CPD trials and instead use commercially sourced aerogel monoliths for subsequent characterization and testing.

3.1.3 Commercial Aerogel Samples Used for Testing

Given the persistent challenges with in-lab drying, monolithic silica aerogel bars were sourced commercially from Ocellus via BuyAerogel.com (Product: Precision Silica Aerogel Bar). These bars are specifically manufactured with precision flat edges and are known as the longest commercially available monolithic silica aerogels. The bars are designed for high optical transparency, thermal insulation, and low-density applications such as science demonstrations and engineering projects. The density of the product is reported as 0.09 g/cm³, and the dimensions are approximately 14 cm × 2.5 cm × 1.0 cm (5.5″ × 1″ × 0.4″). They are available in hydrophilic and hydrophobic formulations; the samples used in this study were hydrophilic. The relevant material properties are summarized in Table 3.1.

Table 3.1 Properties of Silica Aerogel bars

Property	**Value**
Density	~0.09 g/cm³
Thermal Conductivity	~0.02 W/m·K
Transparency	High (visible range)
Porosity	>90%
Dimensions	14 cm × 2.5 cm × 1.0 cm
Formulation type	Hydrophilic

3.1.4 Sample Preparation for Coating and Testing

The commercially purchased monolithic silica aerogel bars were manually cut into smaller rectangular pieces for carbon sputtering and subsequent characterization. To minimize fracture and mechanical damage, a shallow scribe line was first created along the desired cut location using a sharp precision blade. Gentle pressure was then applied along this line to produce a clean, controlled break. This method minimized pore collapse and particle generation while preserving the internal porous structure of the aerogel.

According to the supplier specifications and typical commercial silica aerogel manufacturing methods, the purchased silica aerogels were likely fabricated using a sol-gel process followed by an advanced drying process, such as supercritical CO_2 drying. Therefore, the overall fabrication route was similar to the synthesis approach attempted in this research, although the commercial samples were produced under optimized industrial manufacturing conditions with improved process control and scalability.

Aerogels were cut into smaller pieces with final dimensions of approximately 2.5 cm × 3.0 cm × 1.0 cm for characterization and testing. Only intact and crack-free pieces were selected for further analysis. A thin carbon layer (≈ 500 nm nominal thickness) was deposited onto a designated region of the samples prior to optical and thermal characterization. In addition to these smaller samples, a larger intact piece of carbon-sputtered aerogel (2.59 g) was reserved specifically for CO_2 capture testing. Bare silica aerogel samples (denoted as BSA) and silica aerogel samples with 500 nm of carbon sputtered onto their surface (denoted as CSSA) were retained for characterization and testing, as summarized in Table 3.2.

Table 3.2 Characterization and testing procedures performed on the aerogel samples.

Sample Type	Description / Preparation	Used For
BSA (Bare Silica Aerogel)	Commercially purchased monolithic aerogel bars, cut/snapped into rectangular pieces	UV-Vis Spectroscopy-FTIR Spectroscopy-Photothermal Imaging-CO_2 Capture Test
CSSA (Carbon-Sputtered Silica Aerogel)	Same BSA samples coated with ≈500 nm carbon via magnetron sputtering	UV-Vis Spectroscopy-FTIR Spectroscopy-Photothermal Imaging-CO_2 Capture Test

3.1.5 Carbon Deposition Process Using Magnetron Sputtering

The carbon deposition was carried out using a DC magnetron sputtering system (Angstrom Engineering, Nexdep), located in the York University Microfabrication Facility (YMF) in the basement of the Bergeron Centre for Engineering Excellence. This physical vapor deposition (PVD) technique enables the uniform coating of solid surfaces with high-purity films of controlled thickness under vacuum.

3.1.5.1 Sample Loading and Preparation

Before deposition, the samples were carefully mounted onto a rotating platen (baseplate dimensions: 400 mm × 400 mm) located at the top of the deposition chamber (chamber height: 500 mm), as shown in Figure 3.2 (a–b). Custom clamps were used to secure the fragile aerogel monoliths in place. The samples were oriented facing downward to prevent any loose particles from settling on their surfaces during deposition. The distance between the samples and the carbon target was maintained at ~10 cm, optimized to provide uniform coating while minimizing physical interference with the plasma or deposition zone. Once the setup was complete, the loaded holder was inserted into the chamber, and the pump-down cycle was initiated.

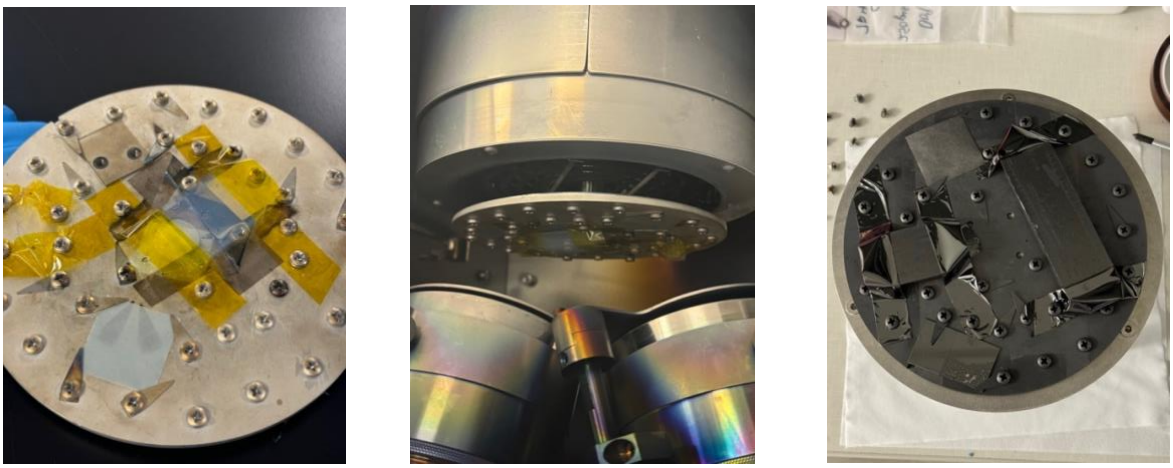

(a) (b) (c)

Figure 3.2 (a) Substrate holder containing bare silica aerogel (BSA) samples secured with Kapton tape and overlaid with carbon templates prior to sputtering. (b) Full top view of the Amod Angstrom Engineering magnetron sputtering system with substrate holder positioned inside the chamber.(c) The same holder after carbon sputtering, showing uniformly coated samples.

3.1.5.2 Deposition Conditions and Process Parameters

The sputtering process was initiated by introducing high-purity argon gas (Ar) into the vacuum chamber as the working plasma medium. The carbon sputtering process was performed at a power of 150 W (DC), under a working pressure of 5 mTorr with an argon flow rate of 20 sccm. The deposition time was 900 s and the target-to-substrate distance was approximately 10 cm. The nominal carbon film thickness (~500 nm) was estimated using the sputter system thickness monitor, which is calibrated based on deposition onto a flat reference surface under identical sputtering conditions. Due to the highly porous and rough morphology of silica aerogels, the local coating thickness on the aerogel surface is expected to vary from the nominal value. Therefore, the reported thickness should be interpreted as an approximate thickness (the thickness that the film would be if it was deposited on a flat surface) rather than a uniform coating thickness across the aerogel surface. A predefined deposition recipe was used, and the deposition conditions are summarized in Table 3.3.

Table 3.3 Sputter Deposition Conditions

Parameter	Value / Description
Target Material	High-purity graphite (99.999%) – 2” diameter, 0.125” thickness (Kurt J. Lesker, CM992.0X0.125-GR)
Power	150 W DC
Working Pressure	5.0 mTorr with 20 sccm argon gas flow
Base Pressure	~1.2×10^{-6} Torr prior to argon introduction
Shutter Condition	Fully open during deposition to allow uninterrupted carbon flux
Substrate Rotation	~5 RPM to enhance uniformity of carbon coating across the aerogel surfaces
Temperature Control	No active heating applied; deposition occurred at ambient temperature to protect aerogel integrity

3.2 Aerogel Characterization

To investigate the structural, optical, and thermal properties of the BSA and CSSA samples, a series of characterization techniques were employed. These included Ultraviolet-Visible (UV-Vis) spectroscopy (Section 3.2.1), Fourier-Transform Infrared (FTIR) spectroscopy (Section 3.2.2), and photothermal imaging (Section 3.2.3). Additionally, a functional performance test for CO_2 adsorption was conducted (Section 3.2.4) and is discussed at the end of this section.

3.2.1 UV-Vis Spectroscopy

The direct transmittance (DT), hemispherical transmittance (HT), and total reflectance (including specular and diffuse reflection) of the BSA and CSSA samples were measured using a Shimadzu UV-2600 spectrophotometer. The measurements were conducted across a wavelength range of 220 nm to 1400 nm, covering the ultraviolet (UV) to near infrared (NIR) regions, and measurements for each sample were repeated three times.

For the measurement of hemispherical transmittance and total reflectance, an integrating sphere coupled with its external detector (Shimadzu ISR-2600 Plus) was utilized. The incorporation of this integrating sphere enabled measurements into the NIR range. Conversely, direct transmittance was measured without the integrating sphere, using the spectrophotometer’s integrated detector.

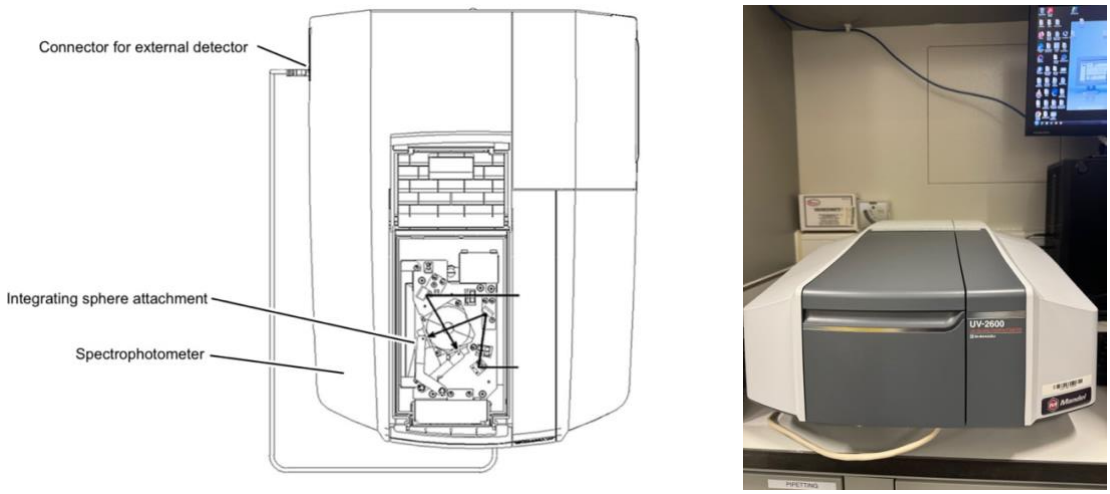

(a) (b)

Figure 3.3 (a) Schematic view of the Shimadzu UV-2600 spectrophotometer with its ISR-2600 Plus integrating sphere attachment. This diagram displays the spectroscopic optical path and sample (SA) placement points for data acquisition. (b) Actual photograph of the Shimadzu UV-2600 spectrophotometer setup used for UV-Vis measurements.

To ensure consistency the UV-Vis measurements were carried out using a similar setup across all samples. This included placing the samples perpendicular to the incident light and positioning the detector on the opposite side to capture the transmitted light. The constant parameters maintained included a 5 mm light beam slit width, a slow scan speed, and a 2 nm sampling interval. The term *"*slow scan speed*"* refers to the rate at which the spectrophotometer records data across the wavelength range; in this study, it corresponds to a scan rate of 200 nm/min. A slower scan speed increases the integration time per data point, thereby enhancing the signal-to-noise ratio and improving spectral accuracy. A precise balance between scan speed and sampling interval was established to reduce noise and ensure the visual clarity and reliability of the acquired data.

The sample/reference (S/R) exchange varied depending on the type of measurement. For transmittance, the S/R exchange was set to normal, while for reflectance, it was set to inverse. Before data acquisition, a baseline correction scan was performed within the designated wavelength range for measurements. As depicted in Figure 3.6, the presence of two white reference plates containing barium sulfate (BaSO4) was essential during the baseline correction scan.

During direct transmission (DT) data acquisition, no external adjustments were made; the measurement was initially conducted without the silica aerogel (SA) sample for the baseline scan, and then continued with the SA sample for actual data recording. The same procedure was followed for hemispherical transmittance (HT) measurements. However, when recording total reflectance (TR), the baseline scan involved both reference plates in place. Subsequently, the reference plate at position 2 was replaced with the SA sample for the measurement.

After each baseline correction scan, data acquisition was performed using UVProbe, the software integrated with the Shimadzu UV-2600 instrument, which enabled the processing and storage of data for further analysis.

Absorbance (A) values were not measured directly but instead calculated using the measured reflectance (R) and transmittance (T) data. The following equation was applied across the UV–Vis–NIR spectrum:

$$A(\lambda) = 1 - R(\lambda) - T(\lambda) \qquad (3.1)$$

This approach ensured consistency across all samples and facilitated the comparison of optical performance based on calculated absorbance.

3.2.2 Fourier Transform Infrared (FTIR) Spectroscopy

All FTIR measurements were performed using a Bruker Vertex 70 FTIR spectrometer equipped with a Pike Technologies integrating sphere. The right-side port of the Pike accessory was used for transmittance measurements, where the IR beam passed directly through the aerogel, while the top-facing port was used to collect the reflected IR signal from the sample surface.

The spectral range spanned 1000–7000 nm, covering both near-infrared (NIR) and mid-infrared (MIR) regions. A gold mirror was used as the reference. The primary purpose of FTIR in this study was to obtain reflectance and transmittance spectra required to calculate absorbance and evaluate the emissivity of the aerogel samples. This information is critical for assessing radiative heat transfer and understanding how carbon sputtering alters the infrared optical response of silica aerogels. All spectra were collected and processed using OPUS software.

For FTIR measurements, a custom 3D-printed sample holder was used to secure the aerogel samples. This holder, fabricated from polylactic acid (PLA) using a Prusa i3 MK3S+ 3D printer,

featured a 4 × 4 cm window to allow for consistent alignment and stable transmission of the IR beam through the sample.

This setup was used consistently to characterize both BSA and CSSA aerogels in NIR (4000–12,500 cm^{-1}) and MIR (400–5000 cm^{-1}) regions. A total of 24 measurements were performed: each sample of BSA and CSSA was tested in both transmittance and reflectance modes, under both NIR and MIR configurations, with three repeated scans per condition. This yields:

BSA: 3 × transmittance (NIR), 3 × transmittance (MIR), 3 × reflectance (NIR), 3 × reflectance (MIR)

CSSA: 3 × transmittance (NIR), 3 × transmittance (MIR), 3 × reflectance (NIR), 3 × reflectance (MIR)

→ Total: 4 conditions × 2 sample types × 3 scans = 24 measurements

Both NIR and MIR spectra were collected using a single DLaTGS detector (deuterated lanthanum-α-alanine doped triglycine sulfate). A quartz beamsplitter was used for NIR, and a potassium bromide (KBr) beamsplitter was used for MIR. Key acquisition settings were standardized to ensure reproducibility: The resolution was set to 8 cm^{-1}, the number of sample and background scans were both set to 1024 scans, and the aperture was 8 mm. The absorbance spectra were calculated from the measured transmittance and reflectance data. The emissivity over the MIR region was calculated as follows:

$$\varepsilon = 1 - T - R \qquad (3.2)$$

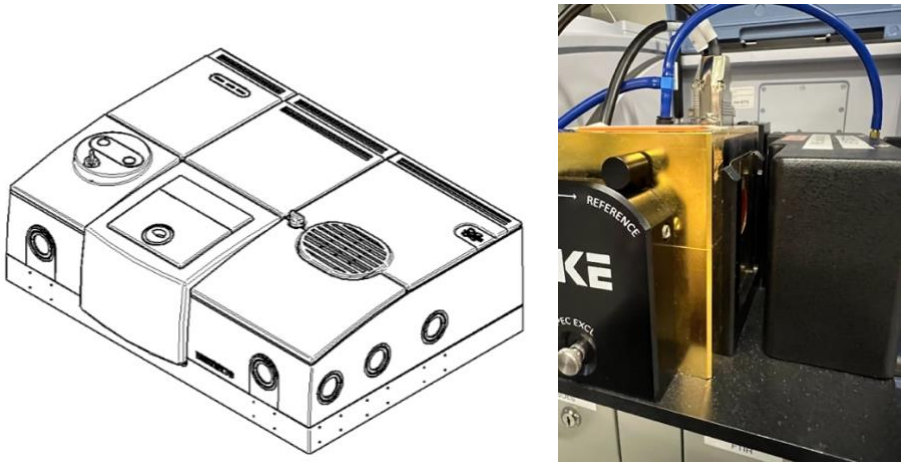

(a) (b

Figure 3.4 (a) Schematic diagram of the Bruker Vertex 70 spectrometer (b) photograph of the Pike reflectance accessory attached to the Bruker Vertex 70 FTIR spectrometer. The top port is used for reflectance measurements; the circular side port on the right is used for transmission measurements.

3.2.3 Thermal Imaging Characterization

The photothermal effect is a phenomenon whereby light is absorbed and converted into heat within a material, causing its temperature to rise. When a material absorbs light, the energy from the photons transforms into thermal energy, leading to an increase in the material's temperature.

A set of two silica aerogel samples, including one Bare Silica Aerogel (BSA) and one Carbon-Sputtered Silica Aerogel (CSSA) was selected for photothermal imaging. These experiments were conducted using a Teledyne thermal imaging camera (FLIR A6750sc MWIR), which operates in the 3000 nm to 5000 nm waveband range.

The experimental setup utilized a 550 W xenon arc lamp solar simulator (Sciencetech SF300-C), positioned directly above the samples. This simulator was supported by a scissor lift, allowing the distance between the lamp and the sample to be adjusted (as illustrated in Figure 3.8). The solar simulator, which illuminates a circular area approximately 5.1 cm (2 inches) in diameter, was accompanied by a 300 W adjustable power supply.

Beneath the silica aerogel samples on the small scissor lift, a reflective, white, PTFE microporous filter sheet was placed. The purpose of this sheet was to reflect light to minimize heat generated in the underlying surface. This precautionary measure aimed to prevent photothermal heat from

being transferred from the platform on the scissor lift to the aerogel sample which would compromise the accuracy of the results.

Throughout all experiments, the intensity of the solar-simulated light incident onto the aerogel samples was maintained at 100 mW/cm² (equivalent to 1 Sun). The distance between the aerogel surface and the xenon arc lamp was fixed at 24 cm to ensure uniform irradiance at the set level for all tests. As shown in Figure 3.8b, the solar simulator was positioned directly above the sample, which rested on a stable platform supported by a scissor lift to allow for precise height adjustment.

The thermal imaging measurements were conducted using a Teledyne FLIR A6750sc MWIR camera operating in the 3–5 µm range. This side-view configuration was intentionally chosen to provide better visualization of heat propagation through the aerogel's thickness, minimize surface glare from the lamp, and capture the internal temperature gradients that would be less visible in a top-view orientation. This approach is especially effective for silica aerogels due to their high porosity and low thermal conductivity, which result in gradual internal heat diffusion.

Each photothermal experiment lasted 30 minutes, including an initial image captured 1 minute after lamp activation, followed by five intermediate images taken at 5-minute intervals (5 min, 10 min, 15 min, 20 min, 25 min), and a final image collected immediately after the lamp was turned off to observe the cooling behavior.

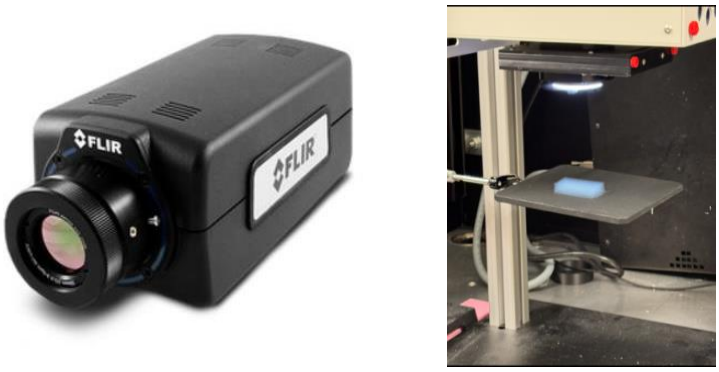

(a) (b)

Figure 3.5 (a) The FLIR thermal imaging camera used in the photothermal experiments. (b) Experimental setup showing the silica aerogel sample placed on a fixed platform beneath the Xenon arc lamp

3.2.4 Carbon Capture Experiment

The carbon capture experiment was conducted on both bare silica aerogel (BSA) and carbon-sputtered silica aerogel with a 500 nm coating thickness (CSSA) to evaluate their comparative performance under identical test conditions.

For the carbon-sputtered silica aerogel (CSSA) two pieces were selected from a single monolithic bar and placed side-by-side in the main chamber. The larger piece weighed 2.59 g with an approximate length of 11 cm, and the smaller piece weighed 0.98 g with a length of about 3 cm, yielding a total sample mass of 3.57 g and a combined length of approximately 14 cm.

For comparison, the BSA sample used in the test was a single uncut bar of the same commercial product (Precision Silica Aerogel Bar, Ocellus Inc.) with approximate dimensions of 14 cm × 2.5 cm × 1 cm and a total mass of 3.36 g, consistent with the manufacturer's specifications (density ≈ 0.09 g/cm³).

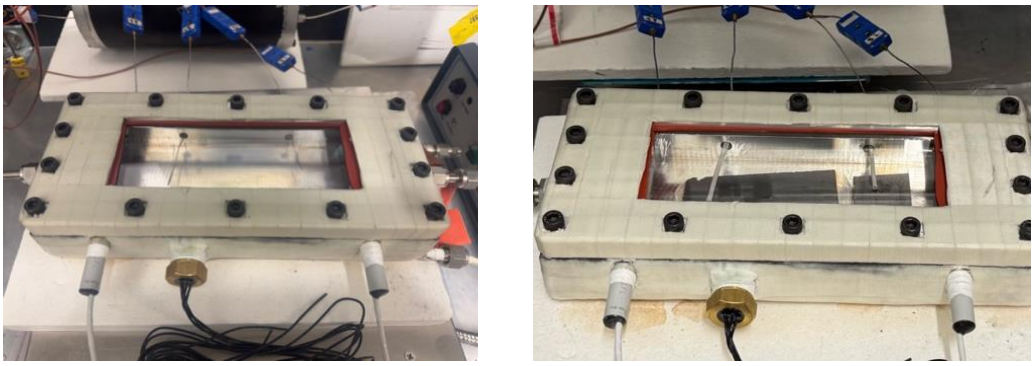

(a) (b)

Figure 3.6 Images of the silica aerogel samples used in the carbon capture test: (a) bare silica aerogel (BSA), and (b) carbon-sputtered silica aerogel (CSSA)

3.2.4.1 Experimental Setup

The CO_2 adsorption and desorption test was carried out using a custom-built gas flow system equipped with two Mass Flow Controllers (MFCs), a heating tape (wrap), a fan for cooling, a CO_2 analyzer, and a series of inlet/outlet valves. The chamber was configured to allow switching between bypass and reaction modes, enabling control over gas exposure to the samples.

A gas mixture comprising approximately 11% CO_2 and 89% N_2 was introduced during the adsorption phase. This concentration was selected based on CO_2 concentrations commonly found in post-combustion flue gas streams from industrial and power plant emissions. The mass flow controllers (MFCs) were adjusted to maintain a constant total flow rate of 111 sccm throughout the test. The heating wrap was used to raise the chamber temperature during the N_2 purge and desorption stages. A fan was used to cool the system to ambient conditions after the heating phases.

The analyzer monitored the CO_2 concentration in real-time, allowing precise observation of adsorption and desorption dynamics.

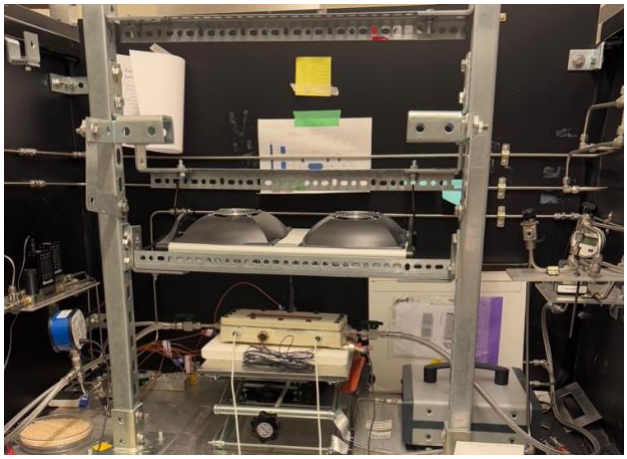

Figure 3.7 Carbon capture setup

3.2.4.2 Procedure for the CO_2 Adsorption/desorption Breakthrough Experiments

The experimental procedure consisted of three main phases: an initial N_2 purge (cleaning), CO_2 adsorption, and thermal desorption. These phases are described below.

3.2.4.2.1 Initial N_2 Purge / Cleaning Phase

The heating wrap and CO_2 analyzer were first turned on. Once the inlet and outlet temperatures reached approximately 100 °C, the N_2 mass-flow controller (MFC) was connected (set to 100 sccm), and the N_2 tank was opened. The system was maintained at 100 °C for 30 minutes to clean and prepare the chamber, with N_2 flowing at a constant rate of 100 sccm. After this 30-minute purge, the heating wrap was turned off and the cooling fan was activated to bring the system back down to ambient temperature.

3.2.4.2.2 CO_2 Adsorption Phase

After the system cooled to ~25 °C, the fan was turned off. The CO_2 tank was opened, and the valves were switched to allow the CO_2 + N_2 gas mixture to pass through the bypass and eventually enter the main chamber. The analyzer reading reached a steady value of approximately 11% CO_2, confirming that the gas flow had stabilized (corresponding to a CO_2 flow of 11 sccm and an N_2 flow of 100 sccm, for a total flow rate of 111 sccm with a relative composition of 11% CO_2 and 89% N_2). Once stable conditions were achieved, the valves were adjusted to direct the CO_2 stream through the adsorption bed, allowing the samples to undergo CO_2 exposure. When the outlet CO_2 concentration reached the same value as the inlet concentration, indicating completion of the adsorption stage, the adsorption bed was isolated by closing both its inlet and outlet valves, and the CO_2 tank was closed.

3.2.4.2.3 Desorption Phase

For desorption, the adsorption bed was gradually heated to approximately 110 °C while N_2 continued to flow through the bypass line. Once the bed reached ~110 °C, the valves were switched so that the N_2 flow (100 sccm) was redirected from the bypass into the adsorption bed. The CO_2 analyzer registered an initial spike—corresponding to the release of adsorbed CO_2—and then gradually decreased toward the baseline level (~0.04%). Following this, the N_2 tank was closed and the heater was turned off, marking the end of the test cycle.

Chapter 4 -Experimental Results

This chapter presents the results obtained from the fabrication and characterization of silica aerogel samples for CO_2 capture applications. The discussion follows the sequence of the experimental procedures described in Chapter 3. Each section outlines the key findings associated with the respective methods, supported by experimental data, graphical analysis, and interpretation.

Section 4.1 focuses on gelation trials during aerogel fabrication, where catalyst concentration and aging time were varied to evaluate their effect on gelation time. Section 4.2 presents the results of optical and thermal characterization techniques, including UV–Vis spectroscopy, FTIR analysis, and photothermal imaging, with direct comparison between bare silica aerogel (BSA) and carbon-sputtered silica aerogel (CSSA). These results highlight the impact of carbon deposition on the optical absorption and thermal response of the material.

Finally, Section 4.3 presents CO_2 adsorption–desorption breakthrough experiments to assess the performance of the aerogel samples for carbon capture. Although the measured CO_2 uptake was limited under the current experimental conditions, the results provide a basis for evaluating the role of carbon sputtering and identifying directions for improving adsorption performance in future work.

4.1 Aerogel Fabrication

The gel time as a function of ammonia volume is plotted in Figure 4.1. The results clearly show that increasing the volume of NH_3 significantly reduces the gelation time across all catalyst aging conditions, confirming the role of ammonia as a base catalyst that accelerates condensation reactions in the sol–gel process. Catalyst aging time also had a strong influence on gelation behavior: the longest aging condition (300 s) resulted in the slowest gelation times at every ammonia volume, as older catalyst solutions undergo partial deactivation and reduced catalytic efficiency. In contrast, the shortest aging condition (60 s) produced the fastest gelation times,

indicating higher catalytic activity immediately after catalyst preparation. Overall, both NH_3 concentration and catalyst aging time play a significant role in controlling gelation kinetics, with higher ammonia volumes and shorter aging times leading to faster gel formation. These results also have practical implications for larger-scale aerogel fabrication, where shorter gelation times may improve manufacturing efficiency and reduce processing time. However, excessively rapid gelation may also reduce control over network uniformity and final pore structure.

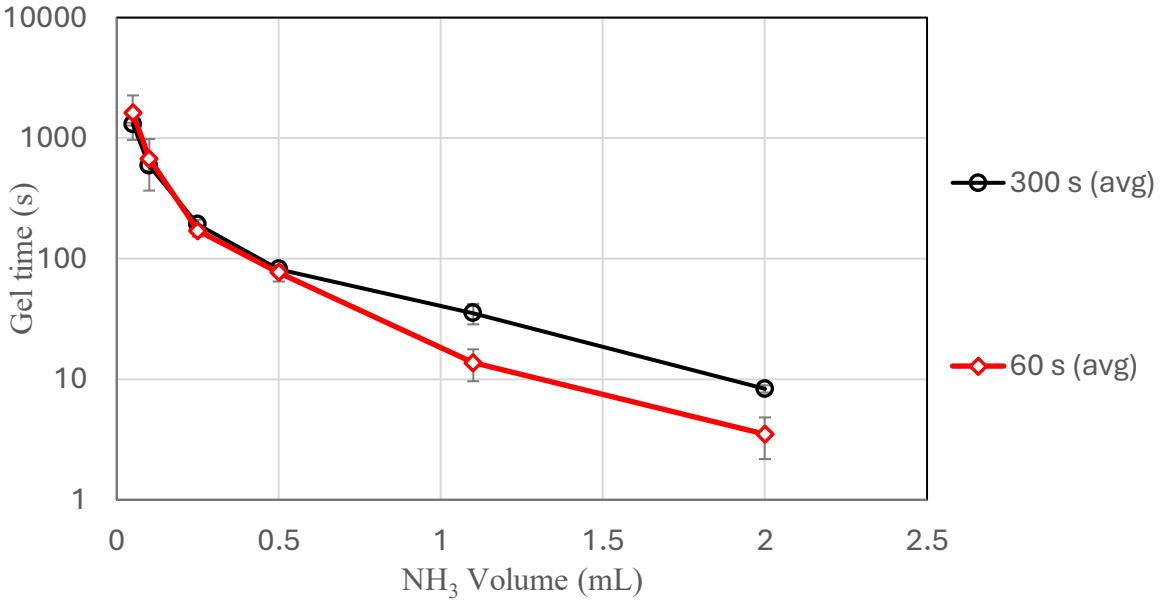

Figure 4.1 Effect of NH_3 volume on gelation time for different catalyst aging times. Error bars represent ±1 standard deviation based on three repeated measurements.

4.1.1 Effect of NH_3 Volume on Gelation Time

As shown in Figure 4.1, regardless of aging time, lower volumes of ammonia (e.g., < 0.5 mL) result in significantly longer gelation times. As the NH_3 volume increases, there is a sharp decline in gelation time. For example, under the 60 s aging condition (represented by the red line), increasing the NH_3 volume from approximately 0.1 mL to 2.0 mL reduces the gelation time from about 1000 s to below 10 s.

This behavior is attributed to the catalytic role of NH_3 in the sol–gel process, where it accelerates the condensation reactions that lead to Si–O–Si bond formation, thus speeding up gelation. The 300 s aging condition (black circles) consistently produced longer gelation times than the 60 s

condition (red line), indicating reduced catalytic activity with increased catalyst aging time. The error bars shown in Figure 4.1 indicate reasonable repeatability between repeated measurements. Although the 60 s condition generally resulted in faster gelation, partial overlap between some error bars suggests that the differences between the two conditions may not be statistically significant at all NH_3 volumes. Individual gelation run data are provided in Appendix A.

4.1.2 Effect of Catalyst Aging Time

Figure 4.1 compares the gelation behavior for two catalyst aging times: 300 s (black circles) and 60 s (red line). In both datasets, increasing NH_3 volume results in shorter gelation times. However, the 60 s aging condition consistently produced lower gelation times than the 300 s condition across all NH_3 volumes, indicating that shorter catalyst aging improves gelation kinetics.

The black and red lines represent averaged values from repeated experiments and demonstrate a consistent trend of decreasing gelation time with increasing NH_3 volume. Overall, increasing the concentration of the base catalyst (NH_3 volume) is the primary factor in reducing gelation time, while shorter catalyst aging times further enhance the gelation rate.

4.1.3 Overall Analysis

Overall, both NH_3 volume and catalyst aging time influence gelation kinetics; however, NH_3 volume is the dominant controlling parameter. Increasing NH_3 concentration leads to a rapid reduction in gelation time, particularly at low volumes where changes result in order-of-magnitude decreases.

In contrast, catalyst aging time has a secondary effect: shorter aging (60 s) results in faster gelation compared to longer aging (300 s). At higher NH_3 volumes (around 2.0 mL), both datasets converge to similarly low gelation times, indicating that the effect of aging time becomes negligible under these conditions.

4.2 Aerogel Characterization

In this section, the characterization results of both bare silica aerogel (BSA) and carbon-sputtered silica aerogel (CSSA) are presented. The BSA samples were commercially sourced, and a uniform carbon coating was applied via magnetron sputtering to enhance surface properties. The analysis includes optical (UV-Vis), spectroscopic (FTIR), thermal (photothermal imaging), and gas

adsorption (CO_2 capture) characterizations to compare the performance of BSA and CSSA in the context of carbon capture applications.

4.2.1 Results from the UV-Visible Spectroscopy Measurements

The UV-Vis reflectance spectra, shown in Figure 4.2, demonstrates clear differences between the BSA and CSSA samples.

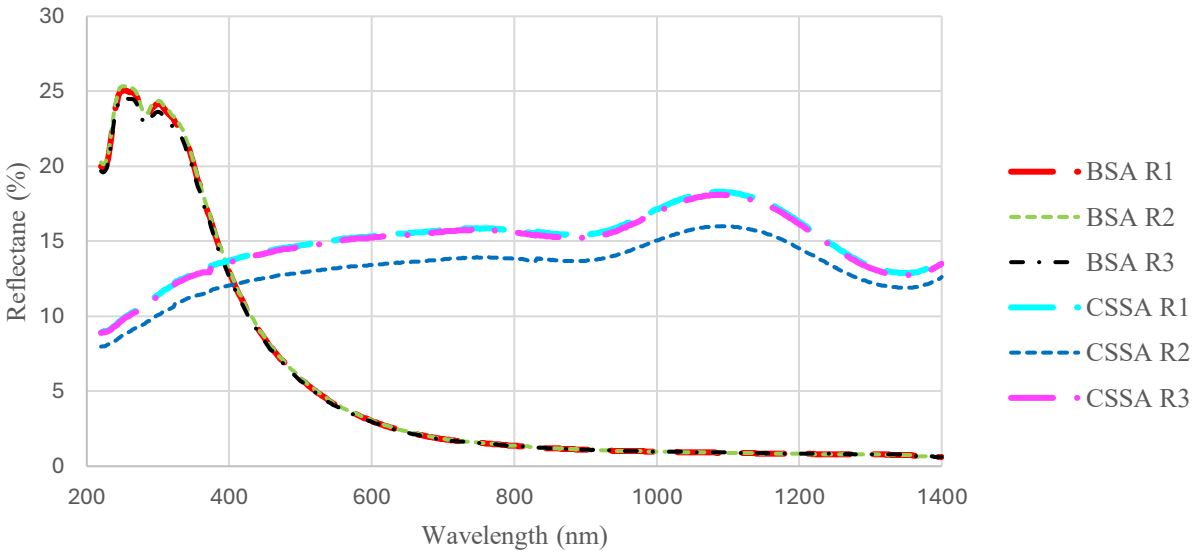

Figure 4.2 Reflectance spectra of Bare Silica Aerogel (BSA) and Carbon-Sputtered Silica Aerogel (CSSA) samples, averaged over three independent runs.

The UV–Vis reflectance measurements for the BSA samples (shown as the red, green, and black lines in Figure 4.2) show a significant reflectance of about 25% at short wavelengths, especially in the ultraviolet (UV) region (around 250 nm). However, as the wavelength increases, the reflectance drops steeply, reaching its lowest value (near zero) in the near-infrared (NIR) region (above 750 nm).

In contrast, the CSSA samples (indicated by the blue and pink lines) exhibit lower reflectance (about 10%) in the UV region. As the wavelength increases, their reflectance gradually rises, reaching a maximum value of about 18% in the near-infrared (NIR) region (1000–1200 nm).

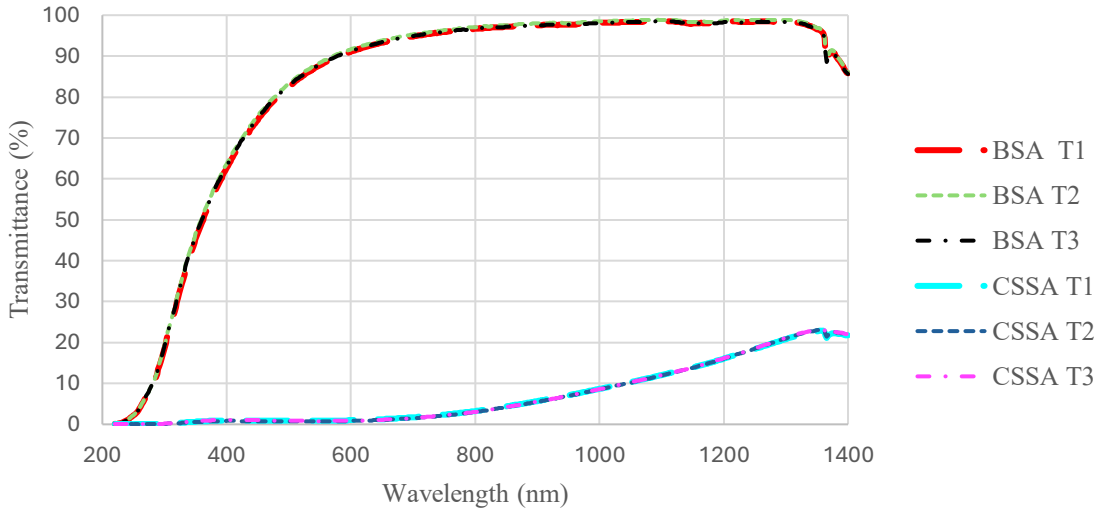

Figure 4.3 Carbon sputtering significantly reduced transmittance overall, indicating that more incident light was absorbed or scattered within the carbon-sputtered silica aerogel. Lower transmittance is desirable for photothermal applications because it allows greater light absorption and heat generation.

The UV-Vis transmittance spectra for the BSA and CSSA samples, shown in Figure 4.3, reveal that the bare silica aerogel maintains very high optical transparency across most of the visible and near-infrared regions, consistent with its porous and highly scattering-resistant structure. However, at lower wavelengths (in the UV region), the transmittance of BSA drops significantly, which is attributed to increased light scattering and absorption by the silica network at shorter wavelengths.

In contrast, the CSSA samples (cyan, blue, and pink lines) show very low transmittance across the entire UV–visible range, with values approaching zero at shorter wavelengths. The transmittance of CSSA increases gradually with wavelength, but only reaches a maximum of approximately 25% in the near-infrared region. This behavior indicates that the carbon coating substantially enhances light attenuation, effectively transforming the material into a strong absorber of both light and heat.

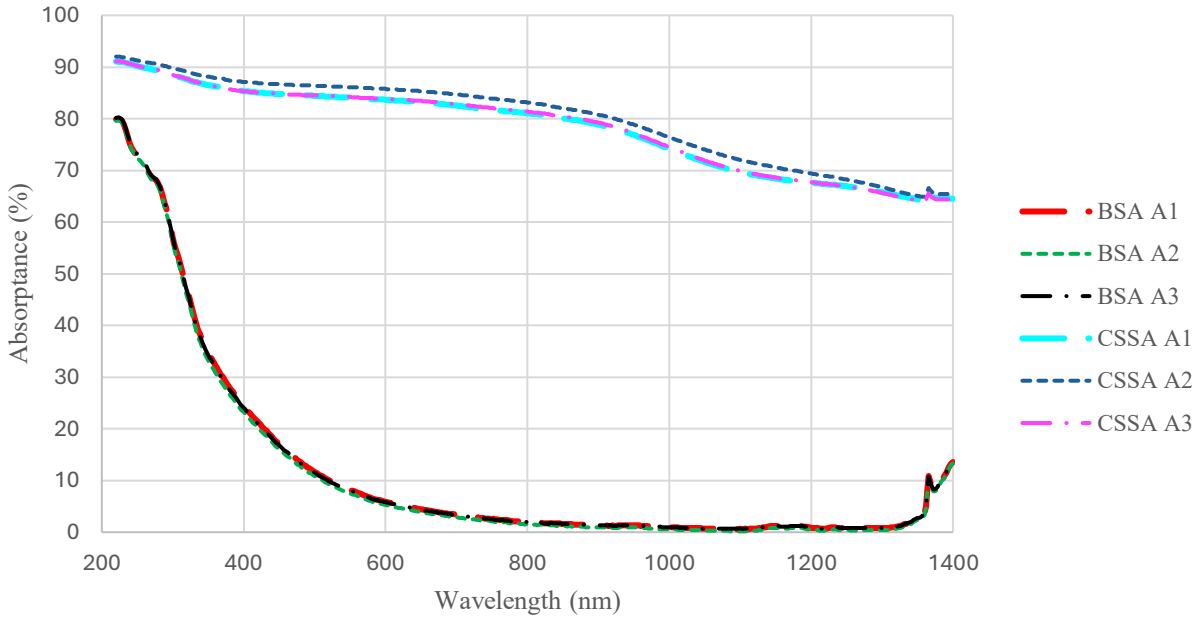

Figure 4.4 Absorptance spectra of BSA and CSSA samples across the 200–1400 nm range, derived from reflectance and transmittance measurements. CSSA exhibits consistently higher absorbance compared to BSA, indicating enhanced optical absorption due to carbon coating.

As shown in Figure 4.4, the absorptance spectra demonstrate that CSSA exhibits significantly higher optical absorption across the 200–1400 nm range compared to BSA. While the bare silica aerogel shows minimal absorption, the carbon-sputtered sample displays enhanced absorptance in both the visible and near-infrared regions, with the most pronounced increase observed at higher wavelengths. This behavior is attributed to the presence of the carbon coating, which increases light absorption and improves photothermal conversion efficiency. These results confirm that carbon sputtering effectively modifies the optical properties of silica aerogels, making CSSA more suitable for applications requiring efficient light-to-heat conversion.

4.2.1.1 Solar Absorption Analysis

To further evaluate the optical performance of the aerogel samples under realistic illumination conditions, the measured absorptance spectra were combined with the ASTM AM1.5 direct solar spectrum. This analysis estimates the fraction of incident solar energy absorbed by bare silica

aerogel (BSA) and carbon-sputtered silica aerogel (CSSA) across the solar wavelength range and provides insight into their solar energy harvesting capability.

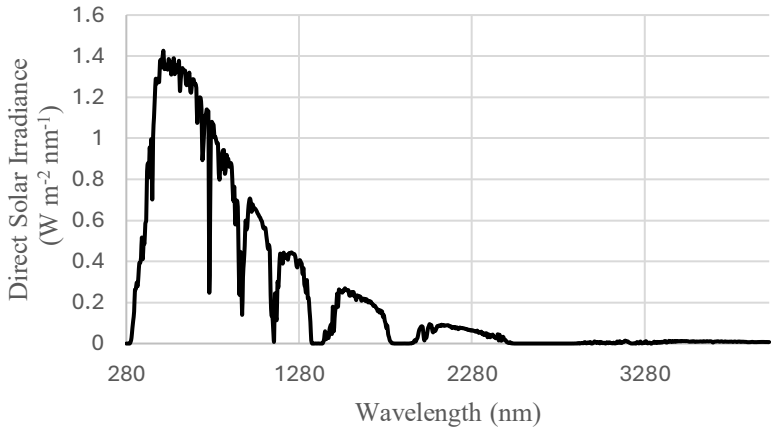

Figure 4.5 ASTM AM1.5 direct solar absorptance calculations.

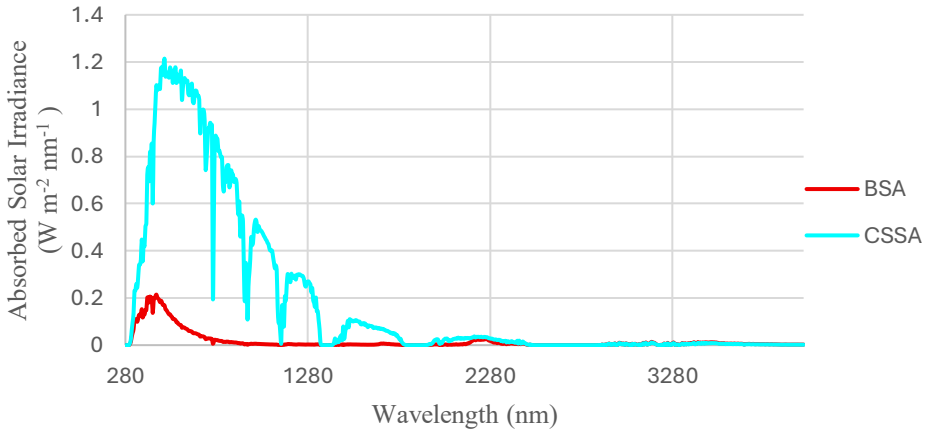

Figure 4.6 Absorbed solar irradiance spectra of BSA and CSSA calculated using measured absorptance and the ASTM AM1.5 solar spectrum.

The calculated solar absorptance values were approximately 6.9% for BSA and 75.8% for CSSA. The significantly higher solar absorptance of CSSA indicates enhanced solar energy absorption following carbon sputtering, consistent with the improved photothermal performance observed experimentally.

The absorbed solar irradiance analysis demonstrates that CSSA absorbs a substantially larger fraction of incident solar energy compared to BSA. The enhanced solar absorptance is attributed to the carbon coating, which increases light absorption across the wavelength range containing the majority of solar irradiance. These findings are consistent with the UV–Vis measurements and support the improved photothermal performance observed for CSSA.

4.2.2 Results from the FTIR Measurements

This research study is focused on investigating the effect of carbon coating on silica aerogels, with an emphasis on understanding their thermo-optical behavior in the infrared region. While UV-Vis spectroscopy provides insight into solar-thermal conversion potential, the FTIR measurements in this study are primarily aimed at evaluating reflectance and transmittance in the mid-infrared (MIR) range to assess emissivity and radiative heat transfer characteristics.

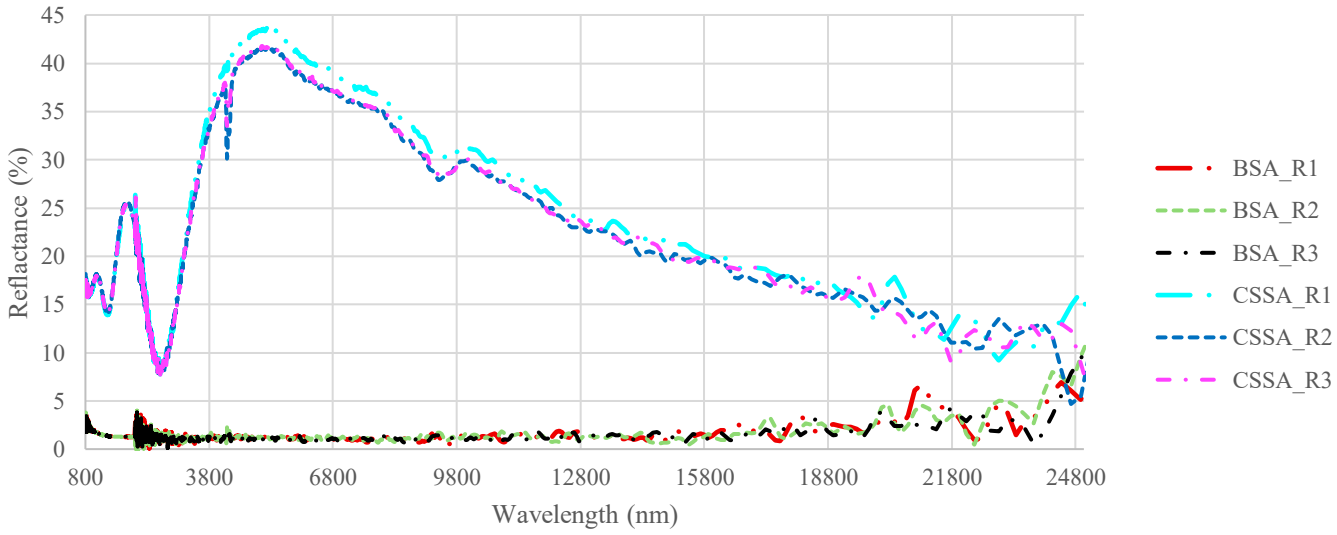

Figure 4.7 FTIR reflectance spectra of BSA and CSSA samples across 800–25,000 nm (three runs each). Carbon sputtering alters the infrared optical response of CSSA, with noticeable changes in reflectance in the mid-IR region.

The FTIR reflectance spectra (shown in Figure 4.5) shows clear differences between the BSA and CSSA samples. The CSSA sample exhibits a different reflectance behavior in the mid-infrared region, indicating that the carbon coating modifies the surface interaction with incident radiation.

This behavior aligns with expectations, as carbon layers typically enhance light scattering and partially block infrared transmission.

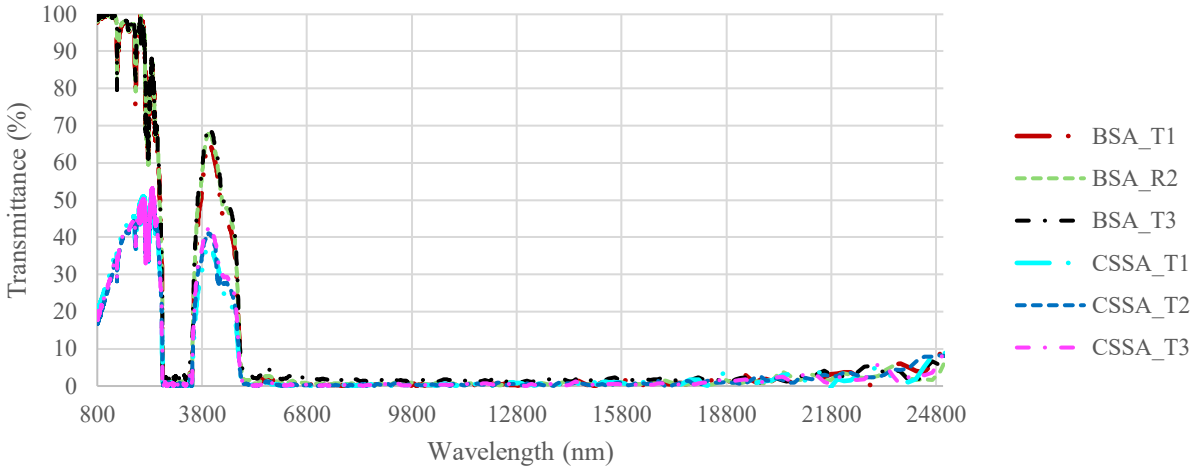

Figure 4.8 FTIR transmittance spectra of BSA and CSSA samples across 800–25,000 nm (three runs each). CSSA exhibits reduced transmittance compared to BSA, consistent with increased optical absorption due to carbon deposition.

The FTIR transmittance spectra (Figure 4.6) further confirms these effects. The BSA sample exhibits consistently higher transmittance than the CSSA sample across the NIR and MIR regions. The reduced transmittance for the CSSA sample corresponds with an increase in absorptance, suggesting that carbon sputtering enhances the photothermal performance of the aerogel by increasing light absorption in both the NIR and MIR regions.

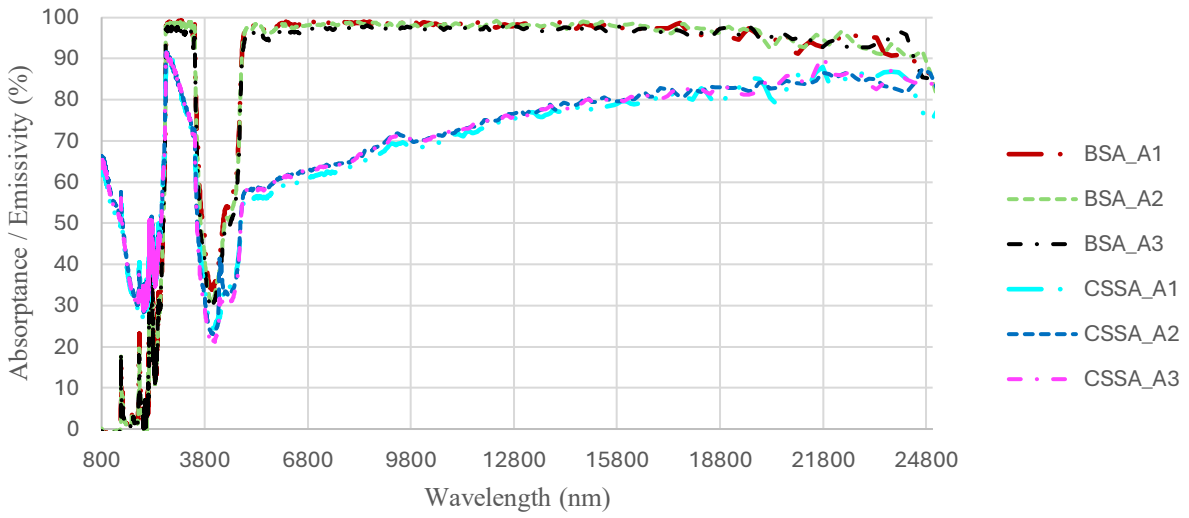

Figure 4.9 FTIR absorptance/emissivity spectra of BSA and CSSA samples across ≈800–25,000 nm. Carbon sputtering enhances absorptance/emissivity in CSSA, indicating stronger infrared attenuation

The FTIR absorptance/emissivity spectra (Figure 4.7) further highlight the differences between the BSA and CSSA samples. The CSSA sample generally exhibits higher absorptance/emissivity across the mid-infrared region compared to BSA, indicating enhanced infrared absorption. In contrast, the BSA sample shows lower absorptance/emissivity and remains less absorbing than CSSA. This behavior is attributed to the carbon coating, which increases infrared absorption and improves the radiative properties of the aerogel. The emissivity of the samples was approximated from the absorptance data, assuming emissivity is approximated as equal to absorptance according to Kirchhoff's law. These results suggest that carbon sputtering enhances the thermal radiation absorption and emission capability of silica aerogels, making CSSA more suitable for applications involving thermal insulation and photothermal energy conversion.

4.2.3 Thermal Imaging

The photothermal behavior of the BSA and CSSA samples were investigated by imaging them with an infrared camera while they were subjected to continuous solar simulated light. Both top-view (surface) and lateral-view (side) thermal images of the samples are presented. The top-view images offer clear insight into the overall heat absorption and surface distribution, while the lateral-view images help visualize the internal heat penetration and retention along the sample thickness.

CSSA (carbon-sputtered silica aerogel, top view)

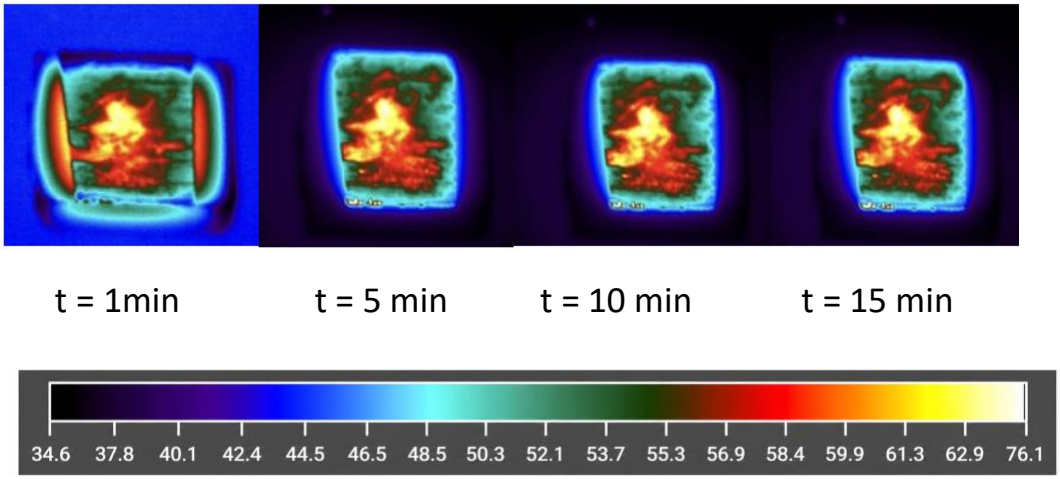

Figure 4.10 Top-view infrared thermal images of CSSA under continuous solar illumination at t = 1, 5, 10, and 15 min. The temperature scale indicates a rapid increase in surface temperature, demonstrating strong photothermal response of the carbon-coated silica aerogel

BSA (bare silica aerogel, top view)

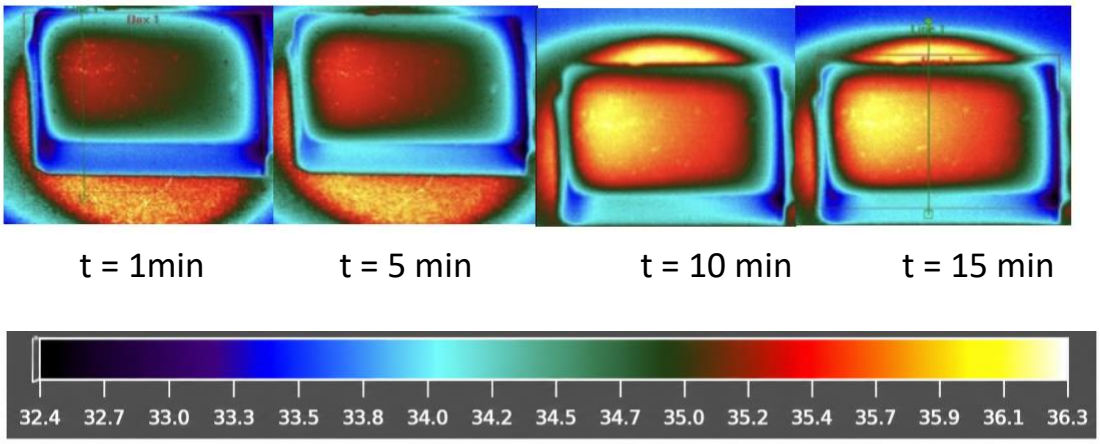

Figure 4.11 Top-view infrared thermal images of BSA under continuous solar illumination at t = 1, 5, 10, and 15 min. Compared to CSSA, the BSA sample shows significantly lower temperature rise compared to CSSA and more uniform heat distribution, indicating reduced photothermal performance.

As shown in Figures 4.8 and 4.9, the CSSA sample exhibits a significantly higher surface temperature than the BSA sample under identical heating conditions.

To complement the top-view images, lateral views were captured to visualize heat penetration through the thickness of the aerogels. The CSSA exhibited stronger heat distribution across the depth compared to BSA, consistent with enhanced optical absorption and improved heat transfer. The following thermal images show side (lateral) views of the aerogel samples over four time points (1, 5, 10, and 15 minutes) during light exposure.

To assess heat penetration and thermal conduction through the thickness of the aerogels, lateral thermal infrared images were taken at multiple time points. For the bare silica aerogel (BSA), heat penetration was initially observed near the surface and gradually penetrated deeper into the sample, with a maximum lateral temperature of ~39 °C reached by 15 minutes. After this point, the temperature distribution stabilized, indicating limited heat diffusion through the thickness due to the material's low thermal conductivity.

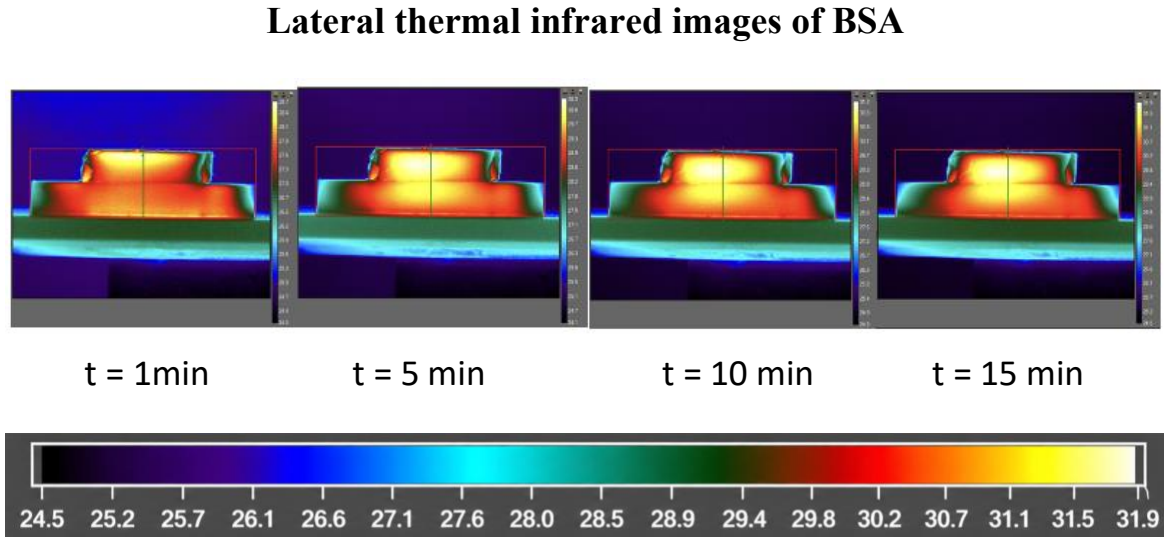

Figure 4.12 Lateral-view infrared thermal images of BSA at (a) 1 min, (b) 5 min, (c) 10 min, and (d) 15 min under continuous illumination. The upper region corresponds to the aerogel sample, while the lower region represents the supporting stage. Heat is primarily localized near the surface and gradually penetrates into the sample with limited depth, indicating low thermal conductivity.

In contrast, the carbon-sputtered silica aerogel (CSSA) demonstrated markedly deeper and more uniform lateral heat penetration. From the early time points (1–5 min), heat distribution across the entire cross-section was more evident, and continued to intensify up to 15 minutes. This behavior

is consistent with the enhanced heat transfer and optical absorption properties introduced by the carbon coating. The stronger lateral heat propagation in CSSA supports the hypothesis that carbon sputtering significantly improves the photothermal performance of silica aerogels by facilitating more efficient heat transfer through the sample thickness.

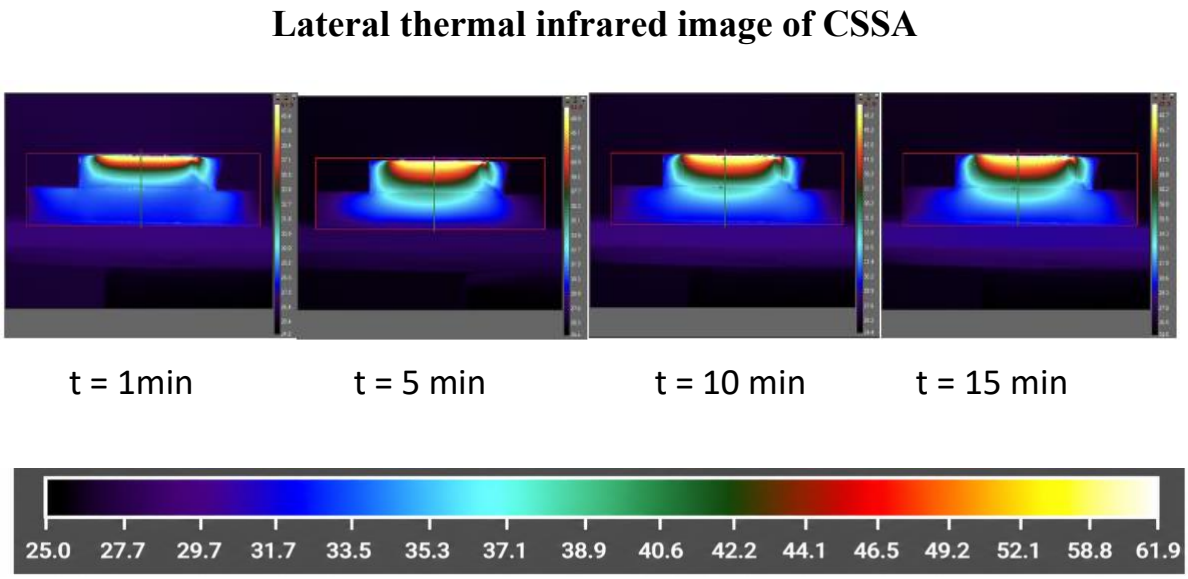

Figure 4.13 Lateral thermal infrared images of CSSA at (a) 1 min, (b) 5 min, (c) 10 min, and (d) 15 min under continuous illumination.

As shown in Figure 4.12, BSA exhibits a gradual increase in surface temperature from ~28 °C to ~39 °C over the course of 30 minutes, reaching a total rise of approximately 11 °C. In contrast, CSSA demonstrates a much steeper and more uniform temperature increase from ~28 °C to nearly 59 °C, with a total rise of over 30 °C within the same duration. The CSSA sample displays not only a higher final temperature, but also a more consistent heating trend, particularly between the 5–20 minute marks. These observations highlight the enhanced photothermal conversion efficiency of CSSA, attributed to the improved optical absorption and enhanced heat transfer. These visual results provide direct qualitative evidence of the superior photothermal response of CSSA, which is further validated by the quantitative temperature data shown in Figure 4.11.

The maximum surface temperature was extracted from the thermal images at fixed intervals. Figure 4.11 and 4.12 show the maximum temperature observed from the infrared images versus time for CSSA and BSA for the top-view and side-view images, respectively.

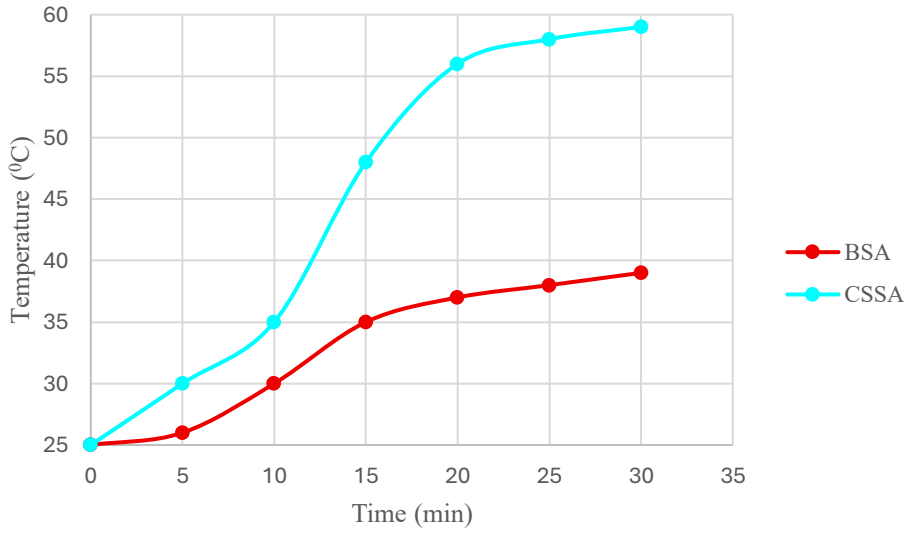

Figure 4.14 Maximum surface temperature versus time for BSA and CSSA samples (top-view infrared measurements). BSA exhibited a gradual temperature rise from ~28 °C to ~39 °C over 30 minutes. In contrast, CSSA showed a sharp increase to ~50 °C within the first 5 minutes, followed by a slower rise, reaching ~59 °C at 30 minutes. The final temperature difference between CSSA and BSA was approximately 20 °C, demonstrating the superior photothermal response of CSSA.

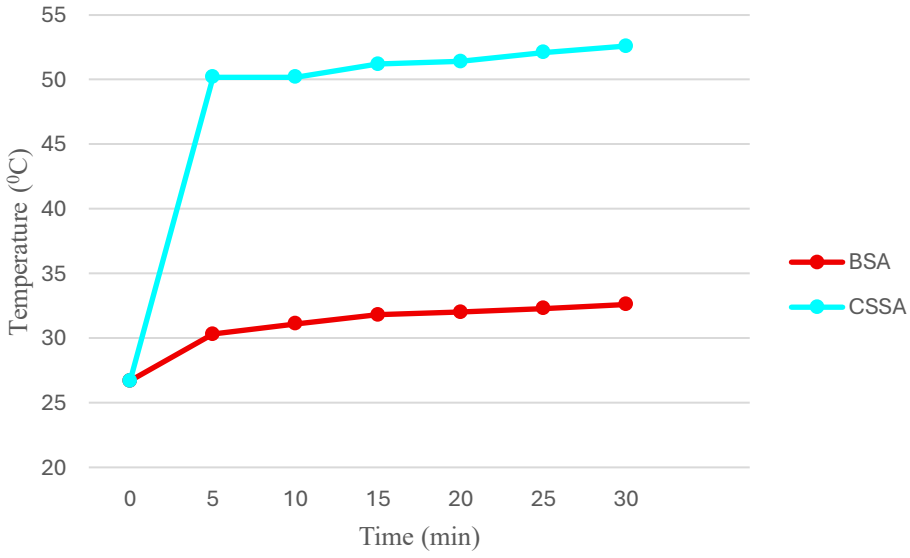

Figure 4.15 Maximum surface temperature versus time for BSA and CSSA samples (side-view infrared measurements). BSA exhibited a gradual temperature rise from ~26.7 °C to ~32.6 °C over 30 minutes. In contrast, CSSA showed a sharp increase to ~50.2 °C within the first 5 minutes, followed by a slower rise, reaching ~52.6 °C at 30 minutes. The final temperature difference between CSSA and BSA was approximately 20 °C, demonstrating the superior photothermal response of CSSA. The slower temperature increase observed at longer heating times does not indicate structural degradation of the sample. Rather, it suggests that the material approaches thermal equilibrium, where heat losses to the surroundings gradually balance heat generation.

Together, these effects explain both the higher peak temperatures and the more uniform heat distribution observed in CSSA compared to BSA. These findings are consistent with prior studies showing that carbon-based modifications to aerogels and other porous nanomaterials can improve photothermal efficiency [17,21,35,44,52].

By validating these results through both qualitative imaging and quantitative thermal data, this study reinforces the role of surface engineering, specifically carbon sputtering, as a scalable approach to enhancing the solar-thermal performance of aerogel-based systems.

This study demonstrated that carbon-sputtered silica aerogels exhibited improved photothermal performance compared to bare silica aerogels. Key findings include:

• Approximately 20 °C higher maximum temperature under identical illumination conditions (59 °C for CSSA vs. 39 °C for BSA).

• Approximately 30% higher optical absorption (~85% vs. ~55%).

• Faster heating response and more uniform thermal distribution attributed to the sputtered carbon layer.

• Reduced light transmittance in the visible and UV spectral regions, transforming CSSA into a stronger broadband absorber.

These findings suggest carbon sputtering as a promising strategy for enhancing the solar-thermal performance of silica aerogels. The results also suggest potential applications in solar-thermal energy conversion, thermal insulation systems, passive heating technologies, and hybrid CO_2-capture/photothermal reactors.

4.2.4 Carbon Capture Experiments

Preliminary adsorption/desorption CO_2 breakthrough measurements were conducted to compare the CO_2 adsorption capabilities of the CSSA and BSA samples. The motivation for this test was to evaluate the potential for surface modification via carbon sputtering to improve the aerogels CO_2 capture performance in a photothermal TSA cycle. Two adsorption/desorption experiments were conducted for the BSA and CSSA samples, and the results are shown in Figures 4.13 to 4.16.

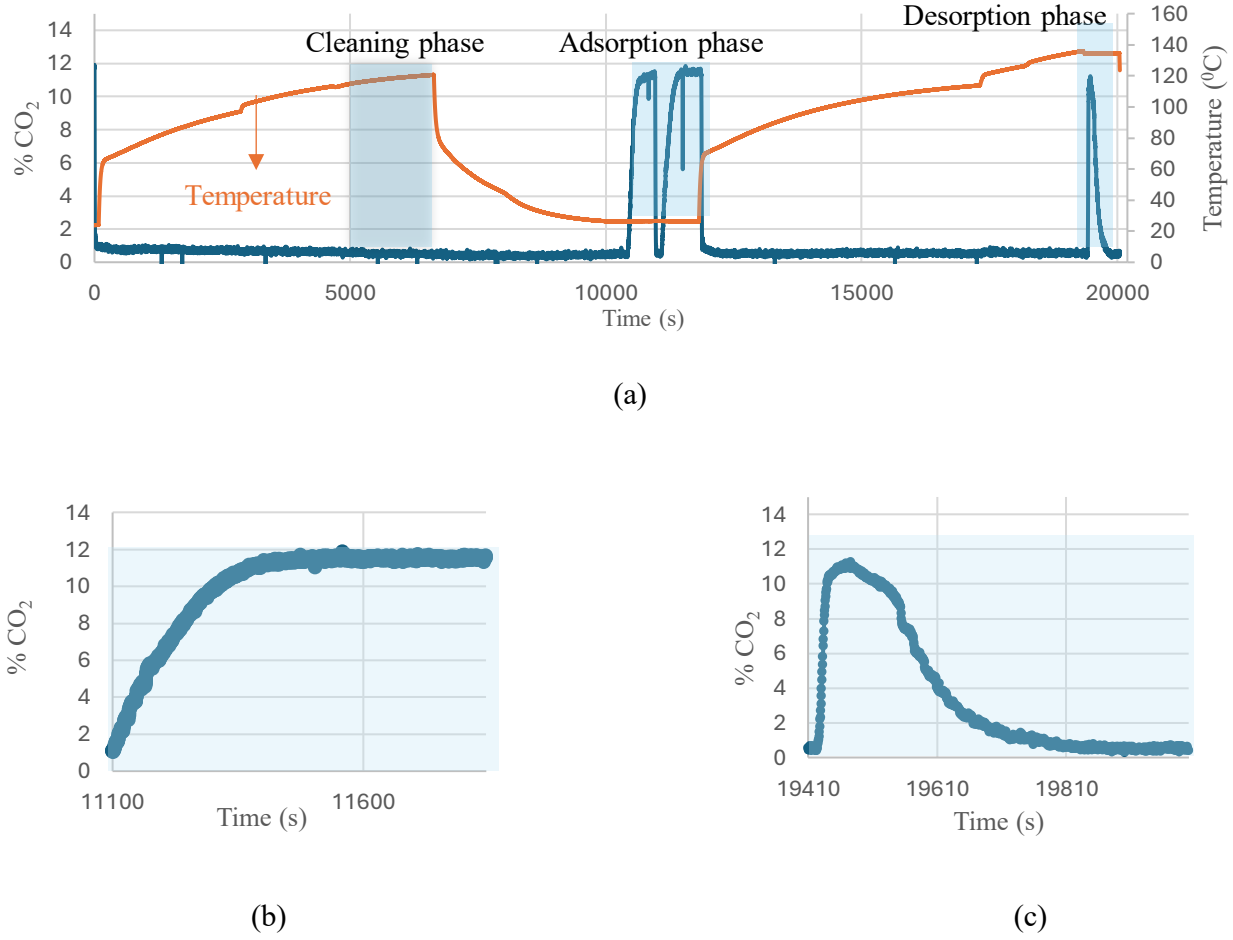

Figure 4.16 CO_2 concentration versus time for BSA (first run) (a) Overall adsorption–desorption cycle; (b) adsorption zoom-in view, (c) desorption zoom-in view.

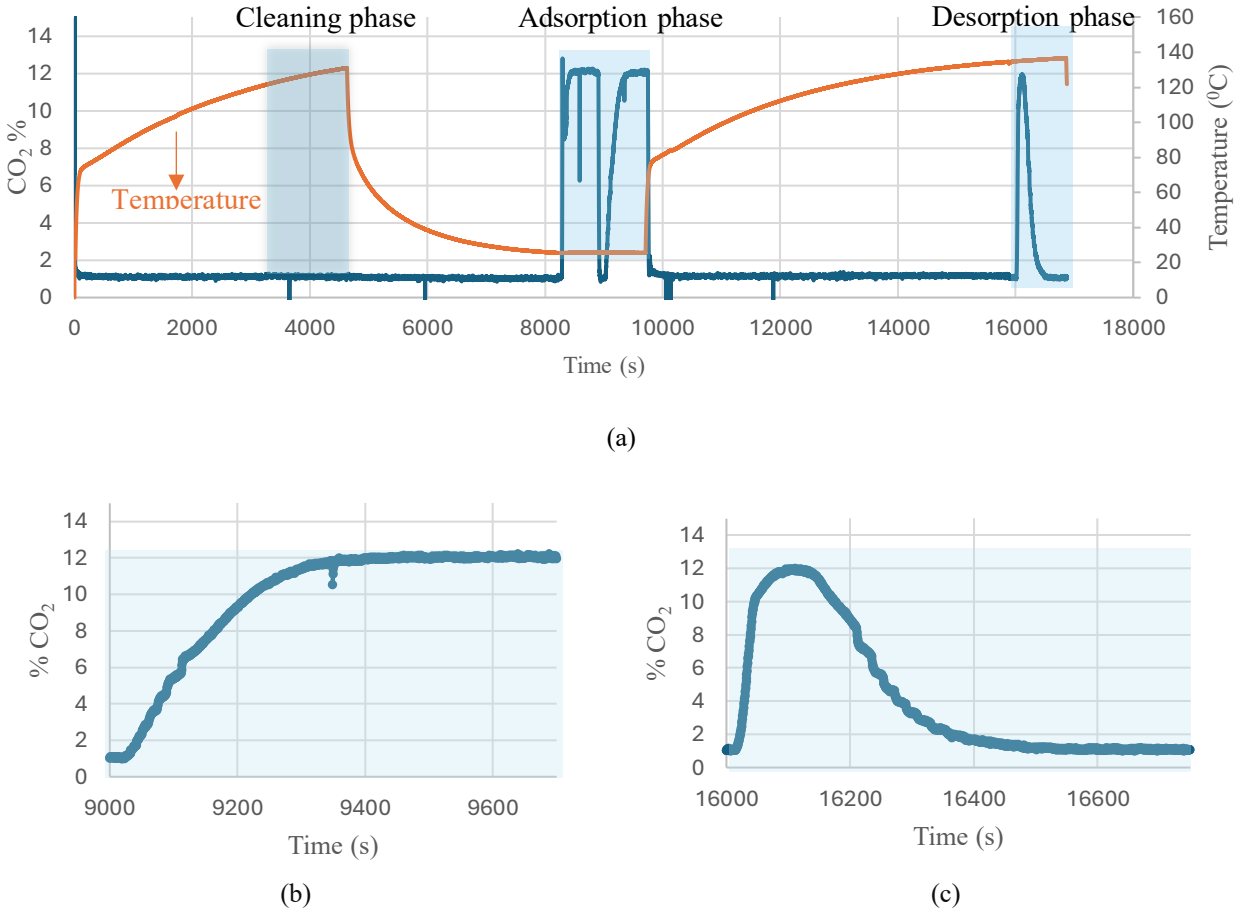

Figure 4.17 CO_2 concentration versus time for BSA (second run) (a) Overall adsorption–desorption cycle; (b) adsorption zoom-in view, (c) desorption zoom-in view.

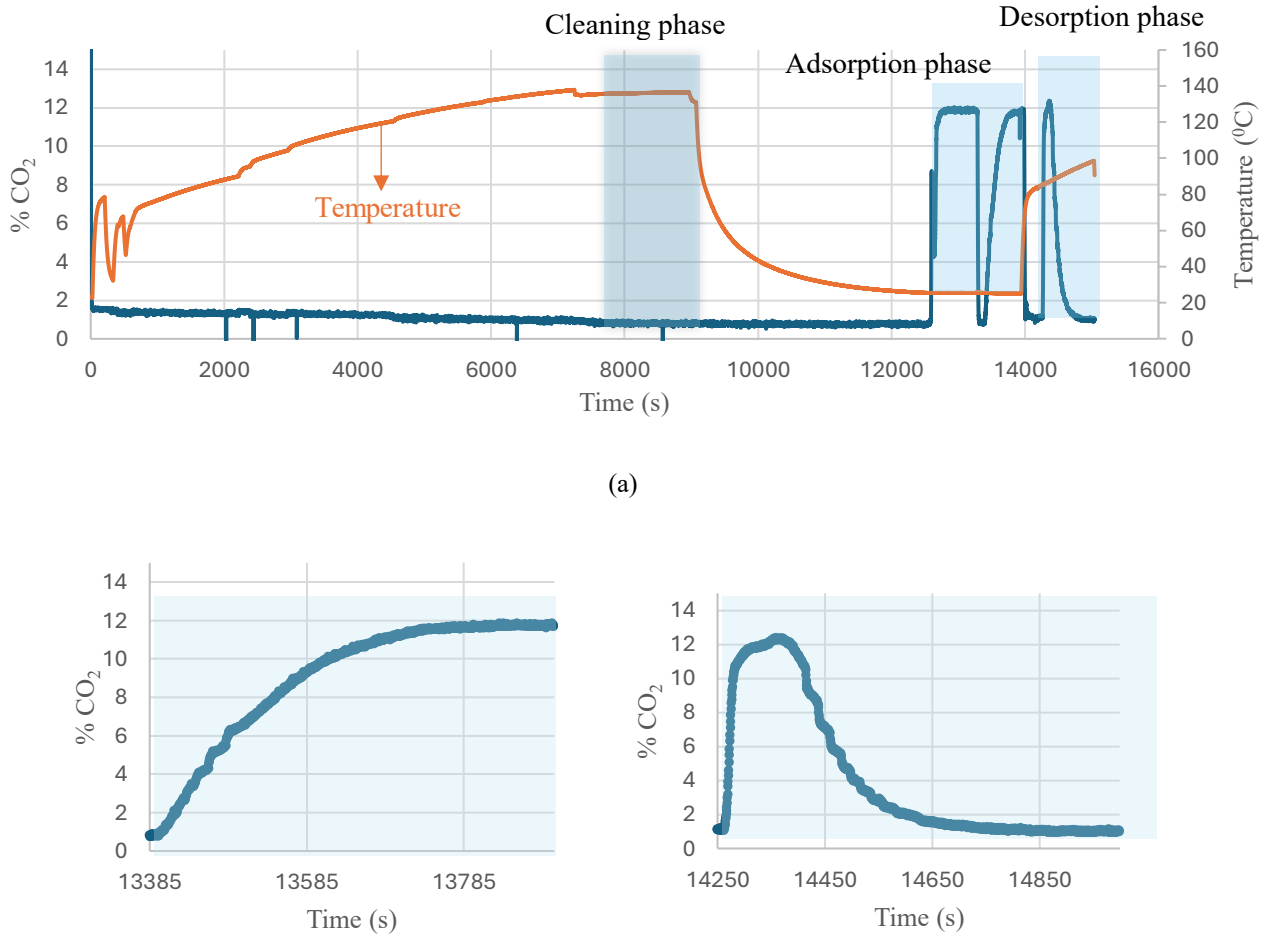

Figure 4.18 CO_2 concentration versus time for CSSA (first run) (a) Overall adsorption–desorption cycle; (b) adsorption zoom-in view, (c) desorption zoom-in view.

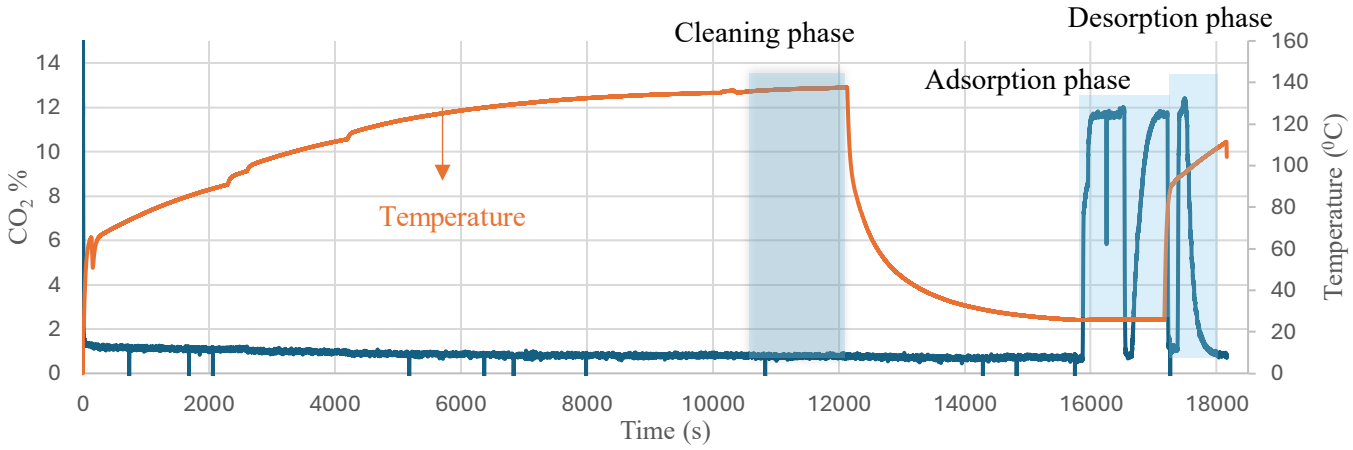

(a)

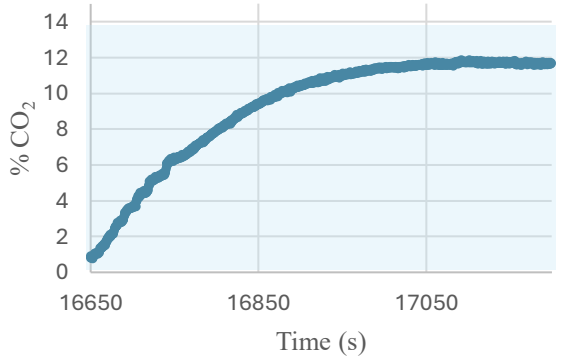

(b)

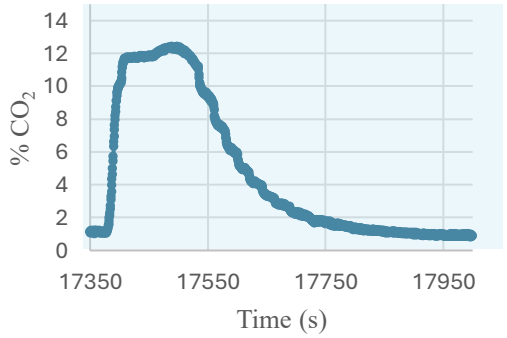

(c)

Figure 4.19 CO_2 concentration versus time for CSSA (second run) (a) Overall adsorption–desorption cycle; (b) adsorption zoom-in view, (c) desorption zoom-in view.

Prior to the onset of the adsorption phase the CO_2 concentration of the feed gas flowing through the bypass is 11%. The adsorption phase is initiated when the valves are switched to direct the feed gas through the adsorption bed. At the beginning of the adsorption phase, an initial drop in CO_2 concentration is observed due to exposure of the fresh adsorption bed to the incoming gas stream. The silica samples initially remove part of the CO_2 from the gas mixture, causing a temporary reduction in the measured outlet concentration. As adsorption sites become progressively occupied, the outlet CO_2 concentration gradually increases until breakthrough occurs.

Following valve switching, the CO_2 concentration rapidly falls to zero. This is because the gas from the adsorption bed, which did not have any CO_2 in it, is directed towards the gas analyzer and because CO_2 from the feed stream is adsorbed by the sample within the adsorption bed. As shown in figures 4.13b, 4.14b, 4.15b, and 4.16b after some time the CO_2 rises back up to 11% as the samples are no longer able to adsorb any more of the incoming CO_2. The area on these figures that is above the adsorption curve and below the 11% CO_2 concentration is used to determine the amount of CO_2 captured (see appendix B).

When the adsorption phase is complete (when the CO_2 concentration reaches and stabilizes at 11%) the composition of the feed gas is changed to pure nitrogen, the adsorption bed valves are closed, and the feed gas is directed through the bypass. To initiate the desorption phase the valves are switched once again to send nitrogen through the adsorption bed. As shown in figures 4.13c, 4.14c, 4.15c, and 4.16c the CO_2 concentration rises and reaches some peak value before decreasing. As the feed gas flowing into the adsorption bed during the desorption phase is nitrogen, the CO_2 exiting the adsorption bed is from the CO_2 that was adsorbed on the sample and that within the volume of the adsorption bed. The adsorption peak exhibits a tail, which is often indicative of slower diffusion from internal pores or residual chemisorbed CO_2, consistent with behavior commonly observed in porous solid adsorbent systems [28,29,31].The gradual decay observed during desorption suggests that CO_2 release is not instantaneous and may be influenced by diffusion limitations within the porous aerogel structure.

The area under the curves in figures 4.13c, 4.14c, 4.15c, and 4.16c is used to determine the amount of CO_2 desorbed (see Appendix B).

The amount of CO_2 adsorbed and desorbed for the four dynamic breakthrough experiments (2 for each of the BSA and CSSA samples) are shown in Figure 4.18. These results indicate that the carbon-sputtered silica aerogel (CSSA) did not show a significant improvement in CO_2 adsorption relative to the bare silica aerogel (BSA)

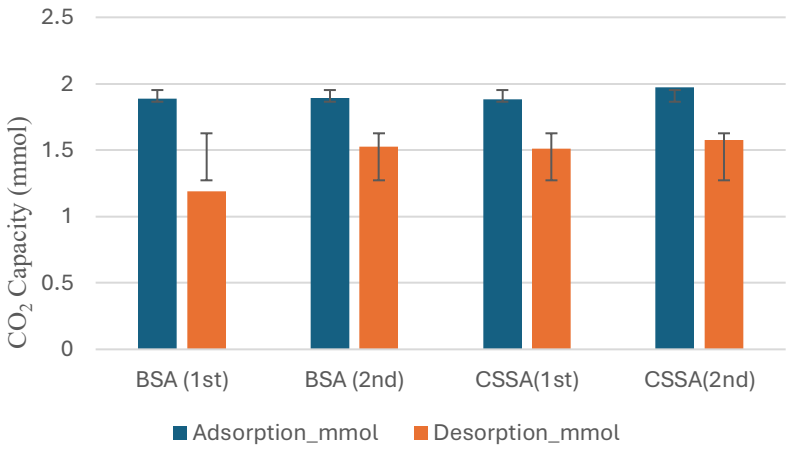

Figure 4.20 CO_2 adsorption and desorption capacity (mmol) for BSA and CSSA samples. Error bars represent ±1 standard deviation based on repeated measurements. A blank run confirmed negligible background CO_2 adsorption (see Appendix C).

It was anticipated that adding a carbon layer on the aerogel surface would increase the number of available active sites and improve CO_2 physisorption through modified surface chemistry. However, the measured uptake capacity, shown in Figure 4.20, did not suggest an obvious enhancement based on the observed adsorption and desorption capacities and associated variability. The carbon layer, optimized for optical absorption, appears to have limited effective porosity and insufficient thickness, preventing sufficient adsorption sites from forming. The thin carbon layer (with an equivalent thickness of a few hundreds of nanometers) likely restricts pore accessibility and active surface area for selective CO_2 binding. Furthermore, the additional sites for adsorption on the carbon layer are relatively small due to how thin this layer. In contrast, adsorption in silica aerogels is often dominated by the intrinsic internal pore network rather than surface-level modification. Thus, the observed adsorption behavior suggests that carbon sputtering alone may not substantially improve CO_2 adsorption performance under the present experimental conditions. Although the carbon coating improved optical absorption and photothermal characteristics observed in earlier experiments, these modifications alone were not sufficient to substantially enhance CO_2 adsorption performance under the present experimental conditions.

4.4.4.1 Limitations of the Carbon Capture Experiments and Suggestions for Future Research

The results attained and presented in the previous section were limited by time for further testing and for fabrication of other advanced aerogel-carbon structures. For example, a preferable configuration may have been to integrate carbon nano particles into the aerogel matrix to increase the number of active sites. Furthermore, future improvements should include:

- CO_2 sorption isotherms at multiple temperatures.
- Assessment of carbon-layer thickness effect on porosity and gas diffusion.
- Integration of chemical adsorbents (e.g., amine-functionalized species such as PEI) into the aerogel network, where the sputtered carbon would primarily serve as a photothermal heating medium during regeneration.

In summary, the BSA sample demonstrated measurable CO_2 adsorption, establishing a baseline for comparison. The CSSA sample, despite its superior optical absorption, did not demonstrate a significant advantage in CO_2 capture, which is attributed to its insufficient thickness and the limited porosity of the carbon layer. Further optimization of coating thickness and incorporation of active adsorbents are expected to improve capture efficiency.

Chapter 5 -Conclusion

This research investigated the optical, photothermal, and carbon capture potential of silica aerogels with and without carbon films sputtered onto their surface. The objective was to evaluate the extent to which the photothermal properties of silica aerogels could be improved by sputtering carbon films onto their surfaces. For this purpose, optical characterization was conducted in the UV-Vis, NIR, and MIR spectra and photothermal behavior was evaluated by imaging the samples with an infrared camera. Furthermore, dynamic adsorption/desorption carbon capture experiments were conducted on the bare silica aerogel (BSA) and on the aerogel with the carbon film sputtered on its surface (CSSA).

Sputtering a 500 nm thick carbon film onto a silica aerogel had a large effect on its absorption. For example, the absorptance of the BSA sample decreases from about 25% to almost zero at 1200 nm, whereas the absorptance of the CSSA sample decreases from about 85% to 70% over the same spectral region. This large increase in absorption improves the photothermal capabilities of the CSSA sample as compared to the BSA sample. For example, after being subjected to solar-simulated radiation for 30 minutes the temperature of the BSA sample reaches 32.6 °C whereas that of the CSSA sample reaches 52.6 °C.

While sputtering carbon layers onto aerogels improved their photothermal properties, dynamic adsorption/desorption experiments revealed that the addition of the carbon films did not noticeably improve their ability to capture CO_2. This result is attributed to insufficient carbon thickness, and reduced pore connectivity after sputtering. Future work will focus on integrating carbon nanoparticles into the bulk of the aerogel samples.

This research also investigated the aerogel fabrication process. Specifically, the effects of aging time and ammonia volume on the gel time was investigated. It was observed that higher ammonia

volumes and shorter catalyst aging consistently producing faster gelation. Ultimately, the successful production of aerogels with desirable final properties (such as insulating performance) requires not only precise fabrication methods (like supercritical drying) but also the accurate control of gelation kinetics through the optimal adjustment of ammonia concentration and catalyst aging time.

Future research should focus on advanced characterization, process optimization, and other potential applications of the photothermal carbon-aerogel composite. Utilizing more advanced techniques like scanning electron microscopy (SEM) and atomic force microscopy (AFM) is essential for a precise investigation of the topology and surface morphology of both aerogels and the carbon film deposited on its surface. Furthermore, current thermal measurements need to be refined. To correct inaccuracies stemming from a constant emissivity value, the true emissivity of the samples should be determined through further FTIR analysis after initial thermal measurements.

With regards to process optimization, a more in-depth exploration of magnetron sputtering mechanisms or experimentation with other forms of physical vapor deposition (PVD) is proposed. This could involve developing a multidisciplinary optimization study to identify and control critical factors influencing material penetration into the aerogel's nanostructure. Attention to sample preparation and strict monitoring of environmental conditions during the process is also vital for understanding the effects of the environment on samples coated with various metals or metal oxides.

While this research serves as a proof of concept, more experimental investigation is needed for the practical implementation of these carbon-aerogel nanocomposites in areas like solar water heating or air and water purification. Given the safer and more environmentally friendly nature of magnetron sputtering, this method could become a more popular option for producing such non-homogeneous nanocomposite aerogels. The ultimate goal of this research is to contribute not only to the academic understanding of aerogels but also to the practical application of these materials in various applications and industries. In addition, the present experiments were conducted under elevated CO_2 concentrations (~11% CO_2 feed gas). Further investigation would be required to determine whether similar adsorption behavior and photothermal regeneration performance could be achieved under atmospheric CO_2 concentrations relevant to direct air capture applications

References

1. Bajoria, A., Kanpariya, J., & Bera, A. (2024). Greenhouse gases and global warming. In *Advances and technology development in greenhouse gases: emission, capture and conversion* (pp. 121135). Elsevier.
2. Rector, T. A. (2024). Consequences of climate change. In *Climate change for astronomers: causes, consequences, and communication* (pp. 4-1). Bristol, UK: IOP Astronomy.
3. Gornall, J., Betts, R., Burke, E., Clark, R., Camp, J., Willett, K., & Wiltshire, A. (2010). Implications of climate change for agricultural productivity in the early twenty-first century. *Philosophical Transactions of the Royal Society B: Biological Sciences*, *365*(1554), 2973-2989.
4. Agreement, P. (2015, December). Paris agreement. In *report of the conference of the parties to the United Nations framework convention on climate change (21st session, 2015: Paris). Retrived December* (Vol. 4, No. 2017, p. 2). Getzville, NY, USA: HeinOnline. 5. Maraveas, C., Karavas, C. S., Loukatos, D., Bartzanas, T., Arvanitis, K. G., & Symeonaki, E. (2023). Agricultural greenhouses: Resource management technologies and perspectives for zero greenhouse gas emissions. *Agriculture*, *13*(7), 1464.
5. Anwar, M. N., Iftikhar, M., Khush Bakhat, B., Sohail, N. F., Baqar, M., Yasir, A., & Nizami, A. S. (2020). Sources of carbon dioxide and environmental Issues. In *Sustainable Agriculture Reviews 37: Carbon Sequestration Vol. 1 Introduction and Biochemical Methods* (pp. 13-36). Cham: Springer International Publishing.
6. Nunes, L. J. (2023). The rising threat of atmospheric CO_2: a review on the causes, impacts, and mitigation strategies. *Environments*, *10*(4), 66.
7. Ooi, Z. L., Tan, P. Y., Tan, L. S., & Yeap, S. P. (2020). Amine-based solvent for CO_2 absorption and its impact on carbon steel corrosion: A perspective review. *Chinese journal of chemical engineering*, *28*(5), 1357-1367.
8. Singh, G., Lee, J., Karakoti, A., Bahadur, R., Yi, J., Zhao, D., ... & Vinu, A. (2020). Emerging trends in porous materials for CO_2 capture and conversion. *Chemical Society Reviews*, *49*(13), 43604404.

9. Water and beyond: expanding the spectrum of large-scale energy efficient separation processes.
10. Kurniawan, T. A., Riaz, M., Mohyuddin, A., Haider, A., Ali, S., AbdulkareemAlsultan, G., ... & Khan, M. M. H. (2024). Inorganic membrane: a game changer for gas separation and purification. *Chemical Papers*, *78*(12), 6787-6820.
11. Yousef, A. M., El-Maghlany, W. M., Eldrainy, Y. A., & Attia, A. (2018). New approach for biogas purification using cryogenic separation and distillation process for CO_2 capture. *Energy*, *156*, 328-351.
12. Sun, M. H., Huang, S. Z., Chen, L. H., Li, Y., Yang, X. Y., Yuan, Z. Y., & Su, B. L. (2016). Applications of hierarchically structured porous materials from energy storage and conversion, catalysis, photocatalysis, adsorption, separation, and sensing to biomedicine. *Chemical society reviews*, *45*(12), 3479-3563.
13. Patel, R. P., Purohit, N. S., & Suthar, A. M. (2009). An overview of silica aerogels. *International Journal of ChemTech Research*, *1*(4), 1052-1057.
14. Zok, F. W., & Levi, C. G. (2001). Mechanical properties of porous matrix ceramic composites. *Advanced Engineering Materials*, *3*(12), 15-23.
15. Patel, R. P., Purohit, N. S., & Suthar, A. M. (2009). An overview of silica aerogels. *International Journal of ChemTech Research*, *1*(4), 1052-1057.
16. Zhu, L., Tian, L., Jiang, S., Han, L., Liang, Y., Li, Q., & Chen, S. (2023). Advances in photothermal regulation strategies: from efficient solar heating to daytime passive cooling. *Chemical Society Reviews*, *52*(21), 7389-7460.
17. Lee, K. H., Arshad, Z., Dahshan, A., Alshareef, M., Alsulami, Q. A., Bibi, A., ... & Javid, A. (2023). Porous aerogel structures as promising materials for photocatalysis, thermal insulation textiles, and technical applications: a review. *Catalysts*, *13*(9), 1286.
18. Vazquez, L., & Buijnsters, J. G. (2009). Chemical and physical sputtering effects on the surface morphology of carbon films grown by plasma chemical vapor deposition. *Journal of Applied Physics*, *106*(3).
19. Mattox, D. M. (2010). *Handbook of physical vapor deposition (PVD) processing*. William Andrew.
20. Lamy-Mendes, A., Silva, R. F., & Durães, L. (2018). Advances in carbon nanostructure–silica aerogel composites: a review. *Journal of Materials Chemistry A*, *6*(4), 1340-1369.

21. Mostafa, M., Antonicelli, C., Varela, C., Barletta, D., & Zondervan, E. (2022). Capturing CO_2 from the atmosphere: Design and analysis of a large-scale DAC facility. *Carbon Capture Science & Technology*, *4*, 100060.
22. Abdulsalam, J., Mulopo, J., Amosa, M. K., Bada, S., Falcon, R., & Oboirien, B. O. (2019). Towards a cleaner natural gas production: recent developments on purification technologies. *Separation Science and Technology*, *54*(15), 2461-2497. 24. Protocol, K. (1997). Kyoto protocol. *UNFCCC Website. Available online: http://unfccc.int/kyoto_protocol/items/2830. php (accessed on 1 January 2011)*, 230-240.
23. Delbeke, J., Runge-Metzger, A., Slingenberg, Y., & Werksman, J. (2019). The paris agreement. In *Towards a climate-neutral Europe* (pp. 24-45). Routledge.
24. Zhang, Z., Borhani, T. N., & El-Naas, M. H. (2018). Carbon capture. In *Exergetic, energetic and environmental dimensions* (pp. 997-1016). Academic Press.
25. Rosenberg, H. S., Curran, L. M., Slack, A. V., Ando, J., & Oxley, J. H. (1980). Post combustion methods for control of NOx emissions. *Progress in Energy and Combustion Science*, *6*(3), 287302.
26. Lee, S. Y., & Park, S. J. (2015). A review on solid adsorbents for carbon dioxide capture. *Journal of Industrial and Engineering Chemistry*, *23*, 1-1.
27. Wang, Q., Luo, J., Zhong, Z., & Borgna, A. (2011). CO_2 capture by solid adsorbents and their applications: current status and new trends. *Energy & Environmental Science*, *4*(1), 42-55. 30.
28. Gurav, J. L., Jung, I. K., Park, H. H., Kang, E. S., & Nadargi, D. Y. (2010). Silica aerogel: synthesis and applications. *Journal of nanomaterials*, *2010*(1), 409310
29. T. Kataoka, Y. Orita, Y. Shimoyama, Photothermal CO_2 desorption from amine-modified silica/carbon aerogel for direct air capture. Chemical Engineering Journal, 782 (2024) 148710.
30. M. Li, J. Xie, P. Tan, J. Liu, C. Gu, X Liu, L. Sun, Precise heating of adsorption sites induced by visible light irradiation, Separation and Purification Technology, 318, (2023) 123968.
31. S. Kar, D. Kim, A. B. M.Annuar, B. B. Sarma, M. Stanton, E. Lam, S. Bhattacharjee, S. Karak, H. F. Greer, E. Reisner, Direct air capture of CO_2 for solar fuel Production in flow, Nature Energy, vol. 10 (2025), 448-459.
32. D. Chuanchuan, L. Yuling, S. Hao, L. Shuaishuai, S. Qiyuan, L. Xinzeng, Evolutionary trends and photothermal catalytic reduction performance of carbon dioxide by MOF-derived MnOx, Fuel, 384, (2025) 133949.

33. T. Sahu, V. Eke, K. K. Ghuman, P. G. O'Brien, Solar-driven photothermal desorption of CO_2 from PEI-infused silica gel, Applied Thermal Engineering, 286 (2026) 129459.
34. X. Zhao, Y. Zhang, M. Zhang, et al., "Harnessing heat beyond 200 °C from unconcentrated sunlight using nonevacuated transparent aerogels," Joule, vol. 3, no. 3, pp. 728–740, 2019.
35. Kistler, S. S. (1931). Coherent expanded aerogels and jellies. *Nature*, *127*(3211), 741-741
36. Yang, J., Wang, H., Zhou, B., Shen, J., Zhang, Z., & Du, A. (2021). Versatile Direct Writing of Aerogel-Based Sol–Gel Inks. *Langmuir*, *37*(6), 2129-2139.
37. Song, B., Liu, J., Feng, X., Wei, L., & Shao, L. (2015). A review on potential neurotoxicity of titanium dioxide nanoparticles. *Nanoscale research letters*, *10*(1), 342.
38. Wang, J., Wei, Y., He, W., & Zhang, X. (2014). A versatile ambient pressure drying approach to synthesize silica-based composite aerogels. *RSC advances*, *4*(93), 51146-51155. 54. Ortiz Ortega, E., Hosseinian, H., Rosales López, M. J., Rodríguez Vera, A., & Hosseini, S. (2022). Characterization techniques for morphology analysis. In *Material Characterization Techniques and Applications* (pp. 1-45). Singapore: Springer Singapore.
39. Sheng, Z., Liu, Z., Hou, Y., Jiang, H., Li, Y., Li, G., & Zhang, X. (2023). The rising aerogel fibers: status, challenges, and opportunities. *Advanced Science*, *10*(9), 2205762.
40. Muhammad, A., Lee, D., Shin, Y., & Park, J. (2021). Recent progress in polysaccharide aerogels: Their synthesis, application, and future outlook. *Polymers*, *13*(8), 1347.
41. Hubáček, T., Siegel, J., Khalili, R., Slepičková-Kasálková, N., & Švorčík, V. (2013). Carbon coatings on polymers and their biocompatibility. *Applied surface science*, *275*, 43-48.
42. Li, X., Zhao, Y., Min, X., Xiao, J., Wu, X., Mi, R., ... & Fang, M. (2022). Carbon nanotubes modified graphene hybrid aerogel-based composite phase change materials for efficient thermal storage. *Energy and Buildings*, *273*, 112384.
43. Yang, W., Liu, J., Wang, Y., & Gao, S. (2020). Experimental study on the thermal conductivity of aerogel-enhanced insulating materials under various hygrothermal environments. *Energy and Buildings*, *206*, 109583.
44. Wang, Y., Wang, R., Liu, L., Xing, C., Guo, Y., Yang, Q., ... & Zhao, C. (2024). Performance analysis of an efficient integration system of coal-fired power plant, solar thermal energy and CO_2 capture. *Journal of Thermal Science*, *33*(4), 1509-1522.

45. Rossnagel, S. M. (2003). Thin film deposition with physical vapor deposition and related technologies. *Journal of Vacuum Science & Technology A: Vacuum, Surfaces, and Films*, *21*(5), S74-S87.
46. Kelly, P. J., & Arnell, R. D. (2000). Magnetron sputtering: a review of recent developments and applications. *Vacuum*, *56*(3), 159-172.
47. Safi, I. (2000). Recent aspects concerning DC reactive magnetron sputtering of thin films: a review. *Surface and Coatings Technology*, *127*(2-3), 203-218.
48. Davidse, P. D., & Maissel, L. I. (1966). Dielectric thin films through rf sputtering. *Journal of Applied Physics*, *37*(2), 574-579.
49. Emmerling, A., Petricevic, R., Beck, A., Wang, P., Scheller, H., & Fricke, J. (1995). Relationship between optical transparency and nanostructural features of silica aerogels. *Journal of noncrystalline solids*, *185*(3), 240-248.
50. Alwin, S., & Sahaya Shajan, X. (2020). Aerogels: promising nanostructured materials for energy conversion and storage applications. *Materials for renewable and sustainable energy*, *9*(2), 7.

Appendices

Appendix A: Individual Gelation Runs

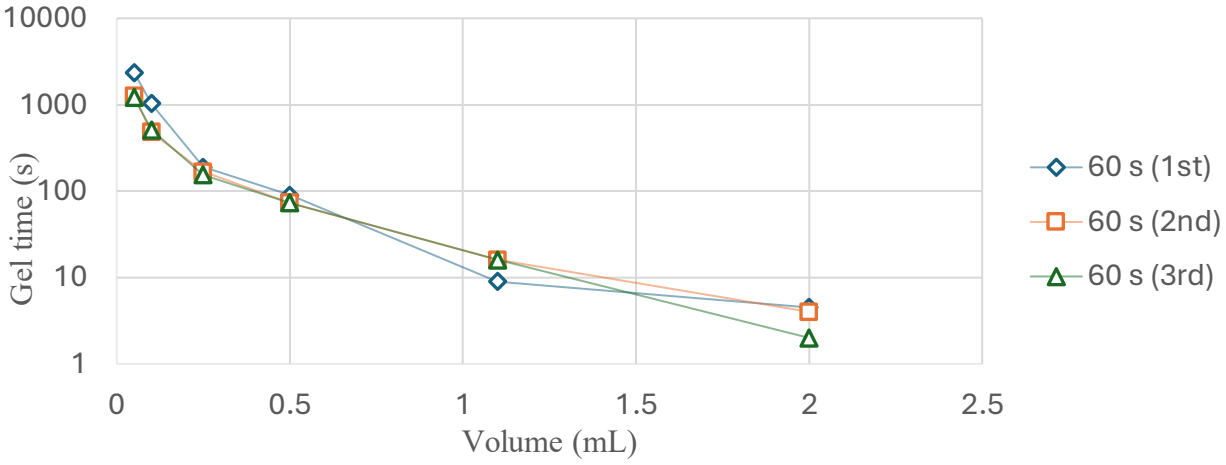

(a)

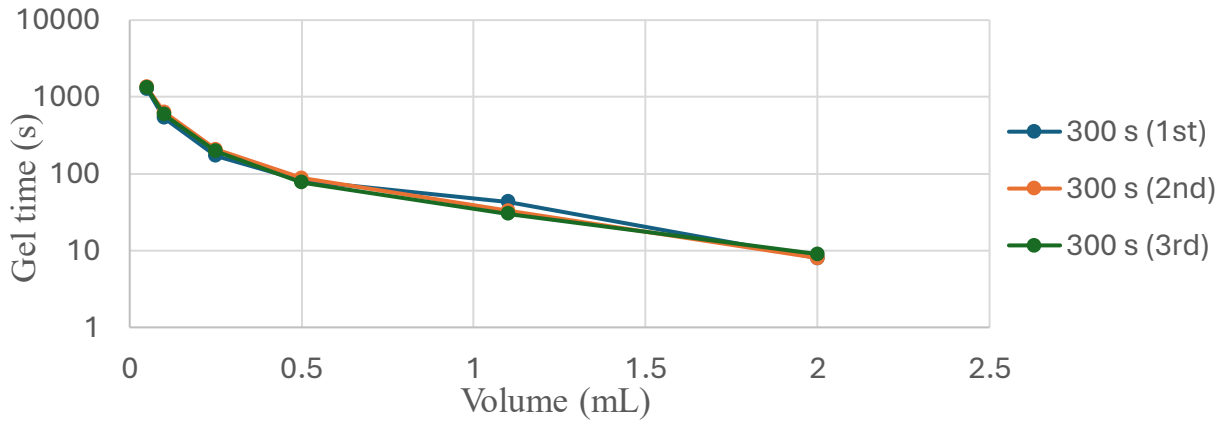

(b)

Figure A1. Individual gelation time measurements for (a) 60 s and (b) 300 s catalyst aging times, showing first, second, and third experimental runs.

Appendix B: Calculation of CO_2 Adsorption and Desorption Capacity

The CO_2 adsorption and desorption capacities were determined from the breakthrough curves by analyzing the variation of outlet CO_2 concentration with time.

The inlet CO_2 concentration was approximately 11%, which was used as the reference baseline. During adsorption, the outlet CO_2 concentration drops significantly as the sample captures CO_2, and then gradually rises back to the inlet concentration once the sample becomes saturated (breakthrough).

To perform the calculation, the CO_2 concentration values were first converted from percentage (%) to fractional form. The amount of CO_2 was then calculated by integrating the difference between the inlet and outlet concentrations over time:

$$n\_CO_2 = \int (C\_in - C\_out) \times Q \times dt / 60$$

where C_in is the inlet CO_2 concentration, C_out is the outlet CO_2 concentration, Q is the total volumetric flow rate (cm^3/min), and t is time.

The integration was performed numerically over the selected time intervals.

The adsorption amount was calculated by integrating the area between the inlet concentration and the outlet concentration curve over the adsorption period.

Similarly, during desorption, when nitrogen is introduced, a sharp increase in outlet CO_2 concentration is observed due to the release of previously adsorbed CO_2. The desorbed amount was calculated by integrating the area under the desorption peak.

The adsorption region and desorption region were identified based on the breakthrough behavior observed in the curves. For example, the adsorption breakthrough region was examined over

approximately 10400–10900 s, where the outlet CO_2 concentration rises from near zero to about 11%, indicating saturation of the sample.

The desorption region was analyzed over approximately 19400–20000 s, where a clear peak in CO_2 concentration is observed followed by a gradual decay. This decay (tailing) indicates slower diffusion from the internal pore structure or partial retention of CO_2.

The measured CO_2 volumes were approximately 46.12 cm^3 for adsorption and 29.05 cm^3 for desorption. These values correspond to approximately 0.002 mol and 0.0013 mol of CO_2, respectively.

The difference between adsorption and desorption values suggests that a portion of CO_2 remains within the material, likely due to incomplete desorption or diffusion limitations within the porous aerogel structure.

These calculated values were used to generate the bar chart presented in Section 4.2.4.

Appendix C: Blank Adsorption–Desorption Runs

Blank adsorption–desorption experiments were performed under identical operating conditions without aerogel samples in the chamber. These tests were conducted to evaluate background CO_2 fluctuations originating from the gas delivery system, chamber volume, tubing, heating process, and analyzer response. The blank runs showed minimal CO_2 response compared to the experiments performed with silica aerogel samples, confirming that the measured adsorption–desorption behavior primarily originated from the tested materials.

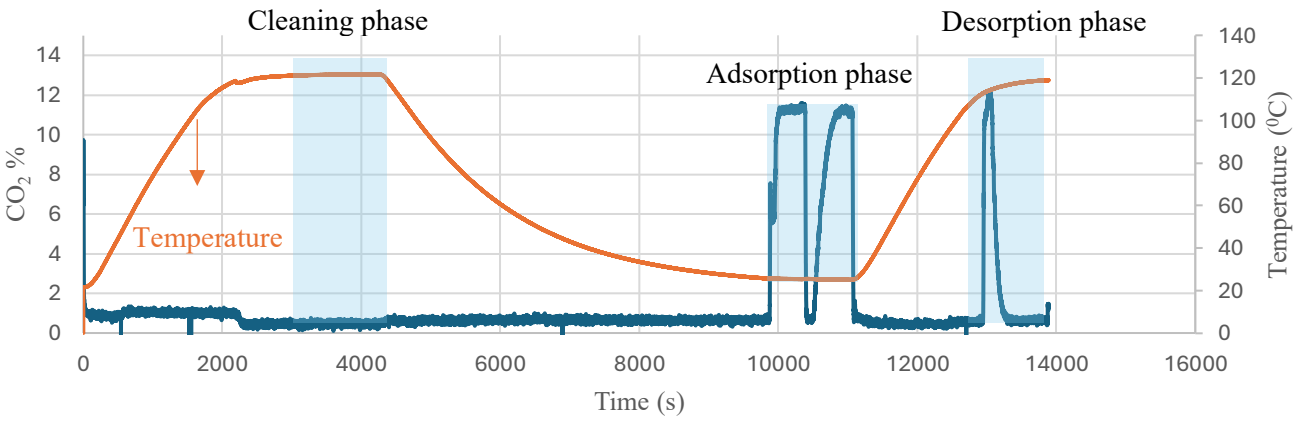

Figure A.2 Blank adsorption–desorption run conducted without aerogel sample under identical gas flow and heating conditions.